# FERROMAGNETISM IN COBALT-DOPED TITANIUM DIOXIDE

by

Alexandre François Lussier

A dissertation submitted in partial fulfillment
of the requirement for the degree

of

Doctor of Philosophy

in

Physics

MONTANA STATE UNIVERSITY
Bozeman, Montana

November 2005

APPROVAL

Of a dissertation submitted by

Alexandre François Lussier

This dissertation has been read by each member of the dissertation committee and has been found to be satisfactory regarding content, English usage, format, citations, bibliographic style, and consistency, and is ready for submission to the College of Graduate Studies.

Yves U. Idzerda

Approved for the Department of Physics

William A. Hiscock

Approved for the College of Graduate Studies

Joseph J. Fedock

## STATEMENT OF PERMISSION TO USE

In presenting this thesis in partial fulfillment of the requirements for a doctoral degree at Montana State University, I agree that the Library shall make it available to borrowers under the rules of the Library.

If I have indicated my intention to copyright this thesis by including a copyright notice page, copying is allowable only for scholarly purposes, consistent with "fair use" as prescribed in the U.S. Copyright Law. Requests for permission for extended quotation from or reproduction of this thesis in whole or in parts may be granted only by the copyright holder.

Alexandre François Lussier

November, 2005

# ACKNOWLEDGMENTS

Several people have contributed to this work. Dr. Yves Idzerda provided the necessary financial support for experiments and travel to conferences, as well as a remarkable freedom to work on research projects of my choice. As my thesis advisor, his extensive knowledge saved me countless hours of web and library searches. Finally, I thank him for his appreciation for all things, physics-related and not. That we have shared opposite ends of a climbing rope on several occasions serves as an indication of my respect spanning beyond professional boundaries.

To my thesis committee members: Dr. Dick Smith, Dr. Recep Avci, Dr. Rufus Cone, and Dr. Hugo Schmidt, I offer my appreciation for their input and careful reading of the manuscript. More generally, I am grateful to the entire MSU Physics Department's faculty and staff, for contributing to a healthy and congenial atmosphere conducive to quality work. Dr. Joe Dvorak is a co-author on all publications related to the work in this dissertation for his assistance in X-ray absorption measurements. His contribution was essential in this work. I am honored to have worked with Dr. Satish Ogale and Dr. Sanjay Shinde from the University of Maryland's Center for Superconductivity Research. They prepared all the samples used in this study, making them indispensable for this work. Additionally, their contagious enthusiasm for physics and dedication to research made them invaluable collaborators.

I thank Susan not only for the tedious task of proofreading the manuscript, but also for being my ski partner, my climbing partner, and my life partner. Finally, I thank my family and friends that have contributed to making this entire process rich and fulfilling.

TABLE OF CONTENTS

1. INTRODUCTION……..... 1

The Advent of Ferromagnetic Semiconductors…….…….. 1
Technological motivation…….……..…… 1
Historical Perspective……..…….……..... 2
Current State of Affairs / Our contributions…..…….…… 3
Dissertation Overview..…….…..... 5

2. X-RAY CHARACTERIZATION TECHNIQUES……...…….…..... 7

General Background…….…….……... 7
Synchrotrons, Synchrotron Light, and Beamlines…… 8
Experiments……..…… 9
X-Ray Absorption Spectroscopy…….……... 9
X-Ray Magnetic Circular Dichroism…….. 12
Experimental Considerations…… 14
The Power of XAS and XMCD Demonstrated…….……... 17
Experimental…….…….. 18
Overlayer Effects on $Fe_3O_4$: TiN…….……... 19
Overlayer Effects on $Fe_3O_4$: $SrTiO_3$ (STO)…….……... 21
Summary…….…… 26

3. MATERIAL CHARACTERIZATION……..…….. 27

Overview……..……. 27
Introduction to Structural Characterization…….. 27
Structural Characterization of Co-doped $TiO_2$……. 28
Introduction……..……... 28
Experimental…….…..... 30
Substrate Temperature During Deposition ……..……..…… 30
Oxygen Partial Pressure During Deposition……..... 32
Cobalt Spectra……..... 34
Film Thickness…….……... 37
Substitutional Nature of Co in Co-doped $TiO_2$ (and $SnO_2$)…….. 37
A few words on $SnO_2$……. 38
Experiment and Results…….. 48
Magnetic Characterization……...……. 43
Lack of XMCD……... 46

TABLE OF CONTENTS – CONTINUED

4. POLARON PERCOLATION MODEL……..……... 50

Previously Proposed Models…… 50
Polaron Percolation Model……...…… 51

5. NON-PERCOLATING-POLARON MANIFESTATION IN XAS……..……... 54

The L* Feature……..... 54
Occurrences of the L* Feature…… 55
Intensity of the L* Feature…….…… 55
Isolated Defect Model…….…….. 57
Defect Model Description…….…….. 57
Origin and Significance of the Effective Defect Radius……..... 61
Polaron / Defect Size Considerations…… 61
Origin of the L* Feature……... 64
Possible Processes……... 64
Substitutional Cobalt and Oxygen Vacancies……..... 68
Vanishing of the L* feature…… 71
The L* Feature and the Magnetic Behavior…….…… 72

6. SUMMARY……..…… 74

Conclusions……... 74
Structural Characterization……..... 75
Magnetic Characterization…….. 75
L* Spectral Feature……..... 76
Future Directions…….. 77
Polaron Radius Confirmation…… 77
XMCD (Lack of…)…….……... 89
Closing Remark……..…….. 80

REFERENCES CITED.....…….……..... 81

# LIST OF TABLES

Table Page

6.1 Polaron Radii of Various Oxides…….…… 77

# LIST OF FIGURES

Figure Page

2.1 The XAS Spectrum of Cobalt……... 10

2.2 The L edge XAS of Octahedrally coordinated $Co^{2+}$……. 11

2.3 Tutorial Figure on XMCD……..... 13

2.4 Iron XAS and XMCD Fe Spectra for $Fe_3O_4$ With Various Thicknesses of TiN Overlayers……. 20

2.5 Iron XAS and XMCD Fe Spectra for $Fe_3O_4$ With Various Thicknesses of $SrTiO_3$ Overlayers……. 21

2.6 Iron XMCD Peak Intensity Versus TiN or STO Overlayer Thickness…… 22

2.7 Normalized Fe XMCD Spectra for $Fe_3O_4$ With Various TiN and STO Overlayer Thicknesses…… 23

2.8 Ferromagnetic ($Fe_3O_4$) and Non-Ferromagnetic (FeO) Components of Iron Oxide Films with TiN Overlayers……. 25

2.9 $Fe_3O_4$ XAS Spectra……... 26

3.1 Titanium and Oxygen XAS Spectra of Co-doped $TiO_2$ Samples Deposited At Various Substrate Temperatures…… 32

3.2 Titanium and Oxygen XAS Spectra of Co-doped $TiO_2$ Samples Deposited In Various Oxygen Partial Pressures……... 33

3.3 Cobalt L edge XAS Spectra of Co-doped $TiO_2$ Samples In the Anatase and Rutile Phases…… 35

3.4 Phase Diagram of Anatase and Rutile Pulse Laser Deposited Structures as a Function of Substrate Temperature and Oxygen Partial Pressure……. 36

3.5 Cobalt L edge Spectra for Co-doped $SnO_2$ (5% and 8%) and Co-doped $TiO_2$ (7%)…… 39

3.6 Oxygen K edge Spectra for Co-doped $SnO_2$ (5% and 8%) and Co-doped $TiO_2$ (Normal and 60° Incidence)…… 41

3.7 Subsequent Hysteresis Loops Measured on Co-doped $SnO_2$..... 42

3.8 VSM Hysteresis Loops for Various Concentration Samples of Co-doped $TiO_2$..... 45

3.9 XMCD and VSM Results on the Same Co-doped $TiO_2$ Sample..... 47

4.1 Superexchange and F-center Exchange Diagrams..... 51

4.2 Illustration of Polaron Percolation Model..... 52

5.1 Cobalt L Edge XAS exhibiting the L* Feature..... 54

5.2 Cobalt L Edge Spectra of Various Cobalt Concentration Samples of Co-doped $TiO_2$..... 56

5.3 L* Spectral Component as a Function of Cobalt Concentration..... 56

5.4 Cobalt L Edge Spectra of Co-doped $La_{0.5}Sr_{0.5}TiO_3$ Deposited In Various Oxygen Partial Pressures..... 57

5.5 Results of Monte Carlo Simulations to Calculate the Fraction of Isolated Defects as Function of Defect Concentration and Size..... 60

5.6 Combined Monte Carlo Simulations and Experimentally Determined L* Spectral Component..... 60

5.7 Calculated Orbital Overlap as a Function of Orbital Separation..... 64

5.8 Possible Lattice Responses to Substitutional Co in $TiO_2$..... 70

5.9 L* Feature Decline and Concurrent Onset of Magnetism In Co-doped Anatase $TiO_2$ as a Function of Co Concentration..... 73

6.1 Expected (Calculated) L* Feature Spectral Component for Various Proposed Co-doped Oxides..... 79

# LIST OF EQUATIONS

Equation Page

2.1 Beer-Lambert Law……...…….…… 15

2.2 Normalized Absorption Intensity.…….…… 16

5.1 Polaron Radius Equation……..…….…… 62

5.2 Polaron Dielectric Constant…….…….…… 62

# ABSTRACT

Semiconductor spintronics is a promising new field of study in the ongoing quest to make electronic devices faster, cheaper, and more efficient. While current spintronics utilizes the spin property of electrons to achieve greater functionality, the integration of spintronics into conventional semiconductor electronics will lead to advances in opto-electronics, quantum computing, and other emerging fields of technology. This integration relies on effective generation, injection, transport, and detection of spin polarized electron currents. To these ends, the successful synthesis of room temperature ferromagnetic semiconductors is mandatory.

In this work, we study the properties of cobalt-doped titanium dioxide, a room temperature dilute ferromagnetic semiconductor discovered in 2001. We characterize the Pulsed Laser Deposition (PLD) of Co-doped $TiO_2$ thin films, including the substrate-induced stabilization of the anatase structure of $TiO_2$. We also confirm the substitutional nature of cobalt on titanium sites by X-ray Absorption Spectroscopy (XAS) techniques.

The ferromagnetic interaction mechanism remains controversial. Yet, we provide experimental evidence for the polaron mediated ferromagnetic coupling mechanism recently suggested to mediate ferromagnetic interactions in this, and other magnetically doped oxides, in the dilute regime (approximately 0 to 3%). Our evidence is related to a previously unobserved and unreported XAS spectral feature. Finally, we demonstrate the surprising absence of an X-ray Magnetic Circular Dichroism (XMCD) signature at the cobalt L edge.

# INTRODUCTION

## The Advent of Ferromagnetic Semiconductors

### Technological Motivation

In the quest for ways to make devices smaller, cheaper, and faster, a promising new field of research is emerging in spintronics[1]. Spintronics is a new and more powerful branch of electronics in which the spin property of electrons, in addition to their charge, is utilized to achieve greater efficiency and functionality. The most common spintronics device is the spin-valve, which is the main component of computer hard-drive read heads. Future advances rely on the integration of spintronics in conventional semiconductor technology, resulting in what has been dubbed: semiconductor spintronics. This new branch of electronics may lead to advances in the fields of opto-electronics, spin quantum devices, and quantum computing[2], but its ultimate success hinges on the resolution of several issues that can be stated broadly as spin generation, injection, transport, and detection.

Ferromagnetic materials are intimately related to spintronics for two reasons. First, the origin of magnetism is largely due to unpaired electron spins. Second, the difference in the density of empty up and down spin states available for conduction above the Fermi level makes ferromagnetic materials suitable as spin filters. This property is utilized in spin-valves and useful for spin polarized current generation. While ferromagnetic metals are adequate for this purpose, their band structure mismatch with semiconductors makes them poor materials for spin injection. The mismatch forces electrons to undergo a scattering event in order to access available electronic states in the

semiconductor. This, in turn, tends to depolarize currents and increase resistivity, causing the interface to act as a spin scatterer[3-6].

A solution to interface spin scattering is the development of ferromagnetic semiconductors that may efficiently generate and inject spin polarized currents. Additionally, their electronic properties may perhaps be tailored to match those of current semiconductor structures. With this in mind, Mn-doped GaAs was successfully used in device structures such as spin polarized light emitting diodes (spin LED) and spin polarized field effect transistors (spin FET)[7, 8], but only at cryogenic temperatures. This poses an obvious problem widespread use in devices. Some success has been achieved specifically for spin injection with the use of insulating tunneling barriers[9] by minimizing the conductivity mismatch at the interface. However, this technique retains a large interface resistance and the development of ferromagnetic semiconductors is still seen as a preferred alternative for integration of spintronics into conventional semiconductor technology[10].

Historical Perspective

Mn-doped GaAs is an example of the early and ongoing efforts with diluted magnetic impurities in III-V semiconductors which produced successful ferromagnetic semiconductors at low temperatures[8]. The search for ferromagnetism in a semiconductor at room temperature was accelerated with the predictions of Dietl *et al.*[11] who performed an exhaustive theoretical study of potential candidate materials in 2000. They notably predicted room temperature ferromagnetism for 5% Mn doped ZnO. Finally, an increased sense of enthusiasm for magnetically doped semiconductors arose with the

discovery of room-temperature ferromagnetism in cobalt-doped anatase $TiO_2$ by Matsumoto *et al*.[12] in 2001, for which they used a combinatorial screening approach.

Current State of Affairs

Since its discovery, Co-doped $TiO_2$ has been studied extensively by several groups. In particular, Chambers *et al*.[13] have been actively characterizing this material by X-ray absorption spectroscopy (XAS), Rutherford Back Scattering (RBS), cross-sectional STM, and various magnetometry techniques. Their work sheds light on the cobalt atoms' valence state and provides a basis for comparison with our XAS spectra. An ongoing controversy surrounding Co-doped $TiO_2$ is determining the mechanism giving rise to ferromagnetism. In 2003 Kim *et al.* claimed that Co clusters in the host structure were responsible for the high temperature magnetic behavior[14]. This was disappointing because it meant that the ferromagnetism was due to a secondary phase, instead of being an intrinsic property of the material, which is desired for spin polarized currents. In the end, there is a consensus that while Co clusters result in a macroscopic ferromagnetic behavior, this doesn't exclude an intrinsic ferromagnetism due to a dilute phase doped semiconductor. Kim *et al.* based their claim on X-ray magnetic circular dichroism (XMCD) studies, in which they failed to detect a ferromagnetic signal until they induced clustering by an annealing process. As it turns out, there is something perplexing about the dilute ferromagnetic semiconductor oxides (DFSO) in that the ferromagnetism does not reveal itself with XMCD. Our combined vibrating sample magnetometer (VSM) and XMCD studies show that cerain samples are evidently ferromagnetic (as evidenced by VSM) yet they show no dichroism. This issue remains unresolved and we will address it in more detail in chapter 3.

Several other studies support the fact that Co-doped anatase $TiO_2$ in which cobalt is well incorporated, (not clustered), is also ferromagnetic[15-17]. Also, looking beyond this one system, groups have experienced various levels of success using a variety of other dilute magnetic oxides with Co or other transition metals as the magnetic dopant[15, 18-24], many exhibiting evidence of room temperature ferromagnetism. In all cases, however, the mechanism leading to ferromagnetism is still in question[8, 11, 15, 22, 25-34].

Conventional ferromagnetic interaction mechanisms are not applicable to several of those systems. Direct exchange is not applicable because the magnetic atoms are dilute (1% to 10%). Therefore, most magnetic impurity atoms are not in close proximity to one another. Near-neighbor interactions between magnetic impurities may occur for some pairs of atoms but is expected to lead to antiferromagnetic coupling[25, 35]. The RKKY interaction has been controversially claimed as a possible interaction mechanism in some of those systems[36]. This interaction mechanism relies on a relatively large charge carrier density but some systems exhibit ferromagnetism in spite of being insulators, rendering this mechanism inapplicable. Recent theories suggest that the presence of oxygen vacancies is a critical component for the development of magnetism in this class of semiconductors[15, 22, 23, 27]. Our observations reflect the importance of oxygen vacancies and we will cover this in chapter 5.

The most recent and arguably most promising model (by Coey *et al.*[27]) is based on polaron percolation. In this model, donor defects are necessary and mediate the ferromagnetism. Polarons are electrons trapped at a donor site in a hydrogen-like orbital. In metal oxides, oxygen vacancies or interstitial cations can result in a polaron. The polaron radius depends on an effective dielectric constant and the effective mass of

electrons in the host material. This radius can be quite large and contain several dopant atoms which couple to the electrons in this polaron. By virtue of their coupling to the polaron electron, the dopant atoms become ferromagnetically coupled to one another. At large enough polaron concentrations the polarons percolate and we obtain a macroscopic ferromagnetic behavior.

Our goal is to elucidate the novel and interesting properties of cobalt-doped titanium dioxide. In particular, we are interested in understanding the still unexplained ferromagnetic interaction mechanism in those materials. Our experimental observations and analysis will provide strong evidence for the presence of polarons thereby supporting the polaron percolation model's validity.

## Dissertation Overview

Our goal is to understand how and why ferromagnetism occurs in cobalt-doped oxides. To this end, we have performed X-ray material characterization and closely examined proposed ferromagnetism interaction models. Our observations provide strong experimental evidence supporting the model proposed by Coey *et al.*[27] We used X-ray Absorption Spectroscopy (XAS) techniques extensively and dedicate chapter 2 to explaining these techniques are explained, along with experimental details. We use XAS to correctly identify the oxidation state of cobalt[37], to identify the host oxide's crystal structure in thin films[38], and to determine the substitutional nature of cobalt atoms in the various oxide matrices[39]. These topics are covered in chapter 3. They show how, even with the lack of success in observing ferromagnetism with XMCD, the X-ray spectroscopy measurements can be used to reveal important characteristics of nearby

atoms and vacancies. At the end of chapter 3, we will also give an overview of our magnetic characterization experiments. Our X-ray absorption studies reveal a surprising and previously unreported feature in the Co L-edge X-ray absorption spectra (XAS) for various cobalt-doped oxides, including Co-doped $La_{0.5}Sr_{0.5}TiO_3$, and Co-doped anatase and rutile $TiO_2$. In our quest to understand the magnetic interactions in the doped oxides, this feature turns out to be very revealing. Its behavior as a function of certain sample parameters is in perfect agreement with the polaron percolation mediated ferromagnetic interaction model, and is covered in chapter 5. Chapter 4 is dedicated to explaining the polaron percolation model in some detail, in preparation for the subject matter covered in chapter 5. In chapter 6 we state our conclusions and discuss further experiments that may be undertaken by future students that could reveal additional useful information.

# X-RAY CHARACTERIZATION TECHNIQUES

## General Background

A number of X-ray absorption spectroscopy techniques (XAS) were used extensively in this thesis and will be described in some detail in this chapter. The basis of the techniques consists of shinning monochromatic light (photons of a well-defined energy) on a sample, and measuring the intensity of light absorbed as a function of photon energy. This implies that the light must not only be monochromatic, we must also have the ability to vary the photon energy in a controlled manner. The light source therefore used for this type of experiment is synchrotron light. The basic workings of a synchrotron will be covered later.

A major guiding concept that makes the technique useful is the presence of absorption edges that are characteristic and unique to each element in the periodic table. The energy at which absorption edges occur indicates which atomic species is absorbing the photons and the spectral shape is characteristic of the chemical and structural environment of the absorbing atom. We thus obtain element specific chemical and structural information regarding the absorbing atoms in the sample. Additionally, the use of right or left circularly polarized photons allows us to independently probe the up and down spin electronic states. Since an imbalance in up and down spin electrons indicates a magnetized sample, the use of right and left circularly polarized light allows us to obtain magnetic information, again with element specificity. This is the basis of X-ray Magnetic Circular Dichroism (XMCD).

Historically, as new phenomena in absorption spectroscopy were discovered, it became necessary to distinguish the absorption techniques in the different absorption regions. Different and complementary information can be gained from the spectral shape near, or in the extended region of the absorption spectra. In this thesis we predominantly use the near edge spectra. This is often referred to as near-edge X-ray absorption fine structure (NEXAFS). Note that the more general designation of X-ray Absorption Spectroscopy (XAS) is loosely and commonly used to discuss the more specific near-edge absorption. The extended region spectroscopy is called extended X-ray absorption fine structure (EXAFS) and can be used to achieve precise structural information regarding the absorption atoms. It is an interesting and powerful application of synchrotron light but was not used extensively in this thesis; therefore, it will not be described in detail.

## Synchrotrons, Synchrotron Light, and Beamlines

Synchrotron light is the light emission from accelerated charged particles. Early spectroscopy experiments were carried out as parasitic experiments around circular particle accelerators but now complete facilities are specifically built for spectroscopy purposes.

The core element of such a facility is the storage ring. Electron bunches are accelerated and then injected in the storage ring, which is an ultra high vacuum tube that has a polygonal footprint. Electrons travel around the storage ring and undergo centripetal accelerations in the bend sections of the tube, thereby emitting light. Acceleration is achieved by the application of a magnetic field perpendicular to the plane

of the ring. So-called insertion devices are also included in the straight sections of the storage ring. These insertion devices consist of arrays of magnets that cause the electrons to undergo an oscillatory motion, thereby generating highly intense and coherent light. Specific designs can additionally control the helicity and ellipticity of the emitted light. An important feature of the design is that electrons travel at a substantial fraction of the speed of light (on the order of 99.999%). Relativistic effects then cause the light to be emitted in a highly focused fashion, in the direction of propagation of the electrons.

Another crucial component of a synchrotron facility is the beamlines. Several beamlines surround the storage ring and their purpose is to effectively use the light emitted at the storage ring to carry out experiments. Light travels along the beamline in ultra high vacuum tubes all the way to the experimental chamber. Mirrors, monochromators, and slits along the beamline allow us to focus the light, adjust the energy, and energy resolution of the photons that reach the sample in the experimental chamber at the end of the beamline. Mechanical, turbo, and ion pumps maintain vacuum in the beamline, and electronic components and computers are used for data acquisition. These components are also considered to be a part of the beamline. Various synchrotrons are dedicated to various photon energy ranges from a few eV to tens of keV.

## Experiments

### X-Ray Absorption Spectroscopy

A variety of experiments can be carried out at synchrotron facilities but only those of interest to thesis will be covered. As photons strike the sample under study, the sample absorbs some photons, reflects some, and transmits the remainder. As the

incident photon energy is tuned to the binding energy of some core electrons of one of the elements comprising the sample, the photon absorption is enhanced due to the additional photon absorption process promoting the given core electrons to empty electronic states above the Fermi level. This leads to a step, known as an absorption edge, in the photon absorption as a function of photon energy. Because core electron binding energies are well defined and unique to each element, the absorbing atomic species can be readily identified by the energy position of absorption edges. After the edge step, the absorption intensity decreases as the more energetic photons interact more weakly with the sample. This is portrayed in Figure 2.1.

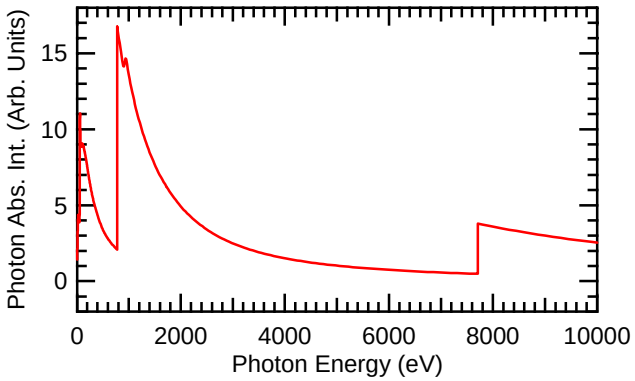


Figure 2.1. XAS spectrum of cobalt from 0 to 10,000 eV.

Within 5 to 10 eV of the absorption edge, the absorption intensity is typically enhanced due to a resonance effect. The photon energy corresponds precisely to the energy difference between the core electronic level from which an electron is excited and the empty electronic states just above the Fermi level. This leads to what is known as the white line demonstrated in Figure 2.2.

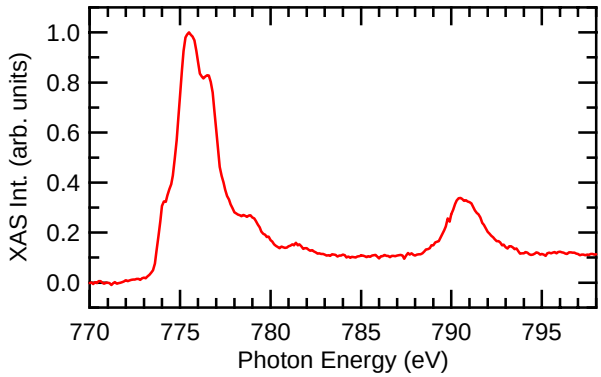


Figure 2.2. $L_3$ and $L_2$ absorption edges of cobalt for 2% Co-doped $TiO_2$. The spectral shape is characteristic of octahedrally coordinated cobalt in the +2 oxidation state.

The white line intensity depends on the electronic transition probability. The $L_3$ edge for example represents a transition from a $2p_{3/2}$ core level to empty 3d states at the Fermi level. The probability of this transition is large according to the dipole selection rules and we correspondingly observe a strong absorption edge. The exact position and shape of the absorption edge are affected by the chemical state of the absorbing atom, in particular, its oxidation state. As a rule of thumb, higher oxidation states cause the absorption edge to shift to higher photon energies because fewer electrons are then shielding the nucleus; thereby increasing the binding energy of the remaining electrons. A shift of a few electron-volts is common. The exact shape of the absorption edge can vary widely for a given atomic species depending on its chemical and structural environment.

In weakly correlated electronic systems the absorption edge's spectral shape is largely determined by the empty electronic state density above the Fermi level. One can calculate the probability of electronic transition from an initial to a final state using the dipole operator on electronic ground states. However, in strongly correlated systems the

creation of a core hole during the absorption process severely distorts the band structure and the spectral shape is dominated by multiplet effects, or end-effects causing a rich spectral structure to arise as shown in the spectrum above.

The spectra can be estimated theoretically but the calculations are quite complex. Theoretical schemes vary for different types of systems, namely, correlated and uncorrelated systems. Experimentalists rarely rely on calculations, and if they do, usually leave this task to theorists. An exception exists relating to Extended X-ray Absorption Fine Structure (EXAFS) analysis where comparison with theory is crucial. However, the theoretical considerations relate not to the shape of the absorption edge, but that of the extended region, which is a result of interference effects on the outgoing electron, not specifically the absorption itself. In this thesis, as in the work of several other authors, I mostly use reference spectra to successfully identify various chemical or structural properties of samples, and variations from one spectrum to another, to reveal useful information regarding samples.

X-Ray Magnetic Circular Dichroism

In order to obtain magnetic information we perform X-ray magnetic circular dichroism (XMCD) experiments. The technique is identical to XAS except that we perform the absorption measurement twice, with left and right circular polarized light. This allows us to selectively investigate the up and down spin populations of a chosen atomic species in the sample. The dipole selection rules state that a dipole transition must occur between electronic states whose orbital quantum number $m_l$ differs by 1. Additionally, if circular polarized light is used, the spin quantum number $m_s$ must change by +1 or -1 depending whether the photon spin is aligned or anti-aligned with the electron

spin. In a magnetized sample, the up and down spin electronic states of the atoms that carry the magnetism are not equally populated; the transition probabilities are accordingly different for up and down spin electrons. Those varying transition probabilities are measured by using right or left circularly polarized light, which result in slightly different spectra. The magnetization is then qualitatively and sometimes quantitatively established by this spectral difference. Note again that this technique is element-specific therefore allowing us to independently probe the magnetization of the different atomic species in a sample.

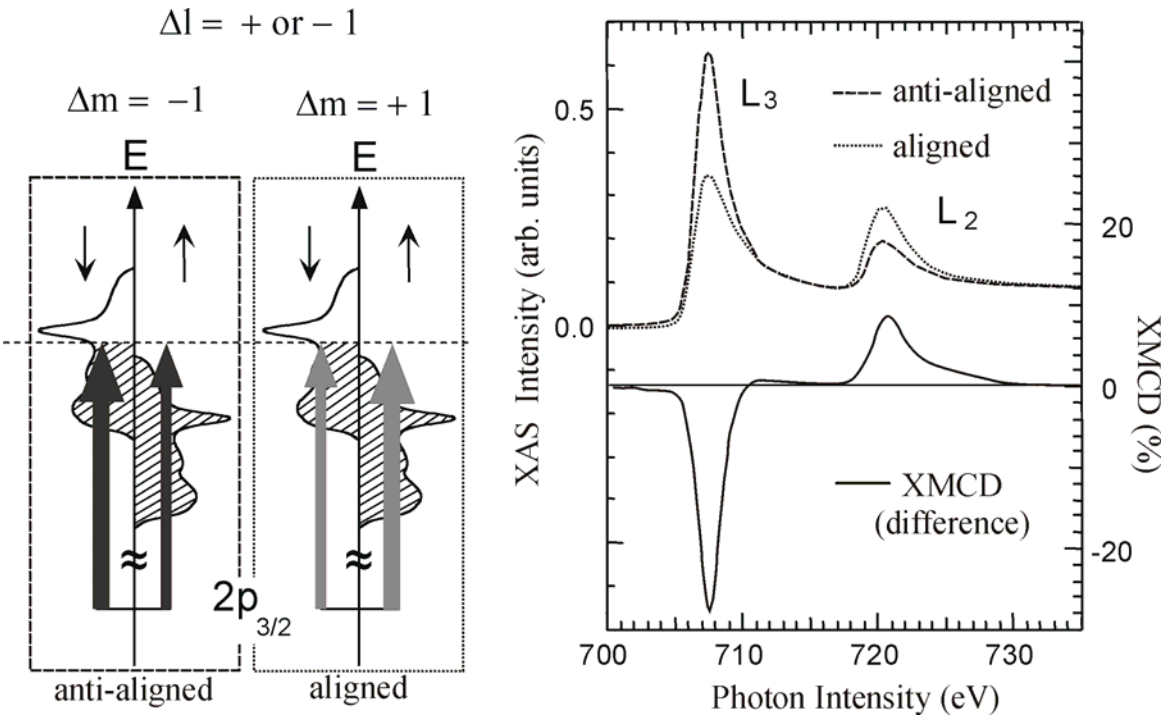


Figure 2.3. (Left) Diagram representing the transition probabilities (arrow thicknesses) at the $L_3$ edge for the two light polarizations, not taking into account the empty states availability just above the Fermi level. (Right) The resulting spectra, which do take into account that the preferred dark grey transition is in fact impossible because there are no states for electrons to scatter into just above the Fermi level. The difference spectrum is shown below in black.

On the diagram above, the arrow thicknesses convey the likelihood of down or up spin electrons being excited from the $2p_{3/2}$ orbital to empty states above the Fermi level ($L_3$ edge). For the case where photon spins are anti-aligned with the sample magnetization, down spin electrons are preferentially excited from the $2p_{3/2}$ to the empty states ($L_3$ edge). When the photon spin is aligned with the sample magnetization, up spin electrons are preferentially excited. However, in the case pictured above, there are no empty electronic states above the Fermi level for up spins to access. The $L_3$ edge is correspondingly smaller.

The pictorial band structure shown above contains no empty states for one of the spin directions (for the up spins). This represents the case for a half-metallic material. This is a special case of ferromagnetism but the material being measured is not required to be half-metallic for XMCD to be observed. An simple imbalance in the up and down spin electronic states, characteristic of a magnetized material, is all that is required to observe XMCD.

## Experimental Considerations

There are several ways to measure the absorption of photons by a given sample. Intuitively, the most obvious way may be to measure transmission. This can be done with a detector that measures the incident photon intensity and the transmitted photon intensity. Experimentally this is a difficult measurement to perform. For soft X-rays, very thin samples are required because the attenuation length of soft X-rays is very short. This is why soft X-ray beam lines and experimental chambers are kept under ultra-high

vacuum, lest the beam intensity would be severely attenuated by air molecules. If this experimental geometry can be achieved, the absorption coefficient μ can be calculated from the Beer-Lambert Law:

$$\mu = \ln(I_o/I_T) \tag{2.1}$$

Typically, we measure thin films deposited on various substrates that are several hundred microns thick, making measurements in the transmission geometry impossible. Therefore, we mostly resort to the total electron yield (TEY) technique. When a photon is absorbed by exciting an electron form a core level to an empty state above the Fermi level or the continuum, a core hole is left behind. This core hole can be filled by various processes such as an Auger process or by an electron dropping into the core hole and emitting a fluorescence photon, which in turn generate photoelectrons. The resultant cascade effect causes several electrons to be emitted from the sample's surface. An indirect way to measure absorption is then to measure the current necessary to replenish the sample. To ensure that emitted electrons do not loop back around to the sample, an extraction grid at a high positive voltage can be held nearby the sample. This is especially concerning if the measurement is carried out in an applied magnetic field. The sample is grounded through a picoammeter to measure the electron yield. To achieve a better signal to noise ratio the picoammeter output signal is converted to a frequency signal whose pulses are integrated over the measurement interval. A reference sample, whose absorption edge position is well known, is typically used to calibrate the energy scale to correct for possible monochromator drift. This is common, namely because of radiation heating and expansion over time. The reference sample is set to intercept a

small edge of the X-ray beam. Next the beam passes through a gold mesh used to measure the incident beam intensity. This reduces the flux by a small amount but is necessary to normalize the measured signal. Finally, a set of horizontal and vertical baffles restricts the size and shape of the beam footprint such that it doesn't spill over the edges of the sample.

When measuring in TEY we take the normalized sample current (divided by incident intensity) to be the absorption intensity.

$$Abs(h\nu) = \frac{I(h\nu)}{I_0(h\nu)} = \frac{Sample \cdot Current(h\nu)}{Gold \cdot Mesh \cdot Current(h\nu)} \tag{2.2}$$

The absorption intensity typically does not correspond directly to the absorption coefficient but is nonetheless the quantity plotted and commonly used for analysis. We plot the XAS intensity (in arbitrary units) versus photon energy. The spectra can be normalized to match the pre and post-edge values of the Henke tables to obtain units in Barns. Still, in cases where there is a large sloping background to the spectra, this procedure is ambiguous because we must perform not only normalizations but also background subtractions in order to match the Henke table values. In this case there is no way, a priori, to know how the intensity of the white line should compare to the edge step. Luckily, arbitrary absorption units are adequate for all analyses we carry out and as long as the analyses are carried out in a consistent manner there is no ambiguity in the results we obtain. In general, the important attributes are the spectral shape and weight distribution, and how the spectra vary from one sample to another.

Regarding background intensities, there is unfortunately nothing than can be done to avoid them entirely; especially in cases where the overall signal is low, for example in

very thin films. There are multiple sources of background. In all current synchrotrons there exists intrinsic decay of the storage ring current resulting in a beam intensity decay. In TEY mode, this should be accounted for in the incident beam normalization, as long as the absorption is a linear function of intensity. More difficult to account for, is time dependent backgrounds related to sample charging or heating. If thin films deposited on insulating substrates are measured, they tend to become electrostatically charged, leading to erroneous intensity measurements. The simple exposure to X-rays can cause sample heating and/or damage that may also affect the absorption properties. In an unpublished study we measured absorption intensity variations of as much as 50% over 10 minutes, at a fixed photon energy (where we would expect the intensity to be constant). The behavior is typically exponential or "double exponential" in time but may also have additional severe behavior at very short time scales. To alleviate this effect we sometimes precede measurements by a wait time (with the X-ray beam on) in order to let the absorption intensity stabilize.

## The Power of XAS and XMCD Demonstrated

We carried out a study with XAS and XMCD that aptly demonstrates the power of the combined techniques of XAS and XMCD to resolve buried interfacial issues. We studied the interface formation between different thicknesses of strontium titanate ($SrTiO_3$) or titanium nitride (TiN) on a 2000 Å $Fe_3O_4$ film. $Fe_3O_4$ is theoretically predicted to be a half metallic ferromagnet, which means it has no down spin electronic states at the Fermi level (100% spin polarized). Experimentally, it has been show to be very close to 100% spin polarized, making it an ideal candidate for use in spintronics

devices. In order to be used effectively in multilayer devices it must be interfaced with other materials. Our results however show that the deposition of 10-50 Å of TiN results in an immediate and substantial removal of oxygen from the near-interface region, resulting in the formation of antiferromagnetic spin-randomizing FeO interlayers. For the deposition of $SrTiO_3$ on $Fe_3O_4$, our measurements show only a small deviation from the $Fe_3O_4$ characteristic XAS signature, suggesting limited formation of perhaps only one monolayer of another Fe oxide at the interface. The persistent XMCD signal, however, confirms the preservation of $Fe_3O_4$ in its near half-metallic state. XAS and XMCD therefore allowed us to successfully investigate a buried interface with element and magnetic specificity.

Experimental

Multiple samples with different overlayer thicknesses were grown by pulsed laser deposition (PLD) at the University of Maryland on $MgAl_2O_4$ substrates. Substrate temperatures were 150ºC for the $Fe_3O_4$ deposition and 200ºC for the overlayer film deposition. The $Fe_3O_4$ thickness was 2000 Å for all samples and the overlayer thickness varied from 0 Å to 48 Å.

The XAS and XMCD spectra were measured at the MSU/NRL Magnetic Materials X-ray Characterization Facility located at beamline U4B of the National Synchrotron Light Source (NSLS) at Brookhaven National Laboratory. The beamline supplies monochromatic, circularly polarized X-rays (in this case, a polarization of 70% was used) in the energy range 20-1350 eV. The monochromator was set at a resolution of 0.25 eV at the Fe $L_{2,3}$ edges. Additional U4B beamline details have been published elsewhere[40, 41].

We record two total electron yield spectra; one with the incident light helicity (circular polarization) oriented parallel to the sample's remnant magnetization and one anti-parallel. The XAS is the average of these two spectra, while the XMCD is the difference between the two. Here, the light helicity was kept constant while the sample remnant magnetization was reversed at each photon energy by reversing a magnetic field applied in-plane with the sample. All XMCD spectra have been corrected for incomplete photon polarization and 45° sample orientation with respect to the incoming beam[42]. With this experimental configuration, our measurements are sensitive to the top 50-100 Å of the $Fe_3O_4$ film. To first order, the presence of the TiN or STO overlayer does not change our probing depth, in spite of decreasing the signal intensity. The results reported here are therefore not due to variations of the probed interfacial volume. Spectra were collected at room temperature and at pressures less than $5x10^{-10}$ Torr.

Overlayer Effects on $Fe_3O_4$: TiN

Figure 2.4 shows the effect of various thicknesses of TiN overlayer deposition on the peak area normalized Fe $L_{2,3}$ XAS and XMCD spectra. As the TiN overlayer thickness increases the spectral weight of the $L_3$ edge shifts to a lower photon energy (approximately from 709 to 708 eV). Simultaneously, the XMCD spectra are observed to decrease in intensity, but remain essentially unchanged in shape. This can only occur if the iron oxide is changing from its ferromagnetic $Fe_3O_4$ form to a non-magnetic structure, such as FeO, with TiN overlayer deposition. The top panel of figure 2.4 shows the XAS results and the bottom panel shows the normalized XMCD.

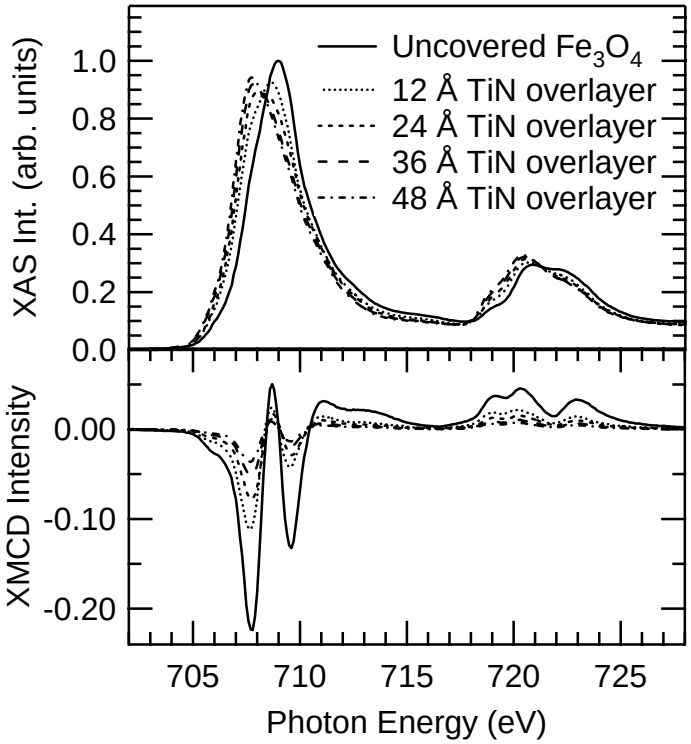


Figure 2.4. The peak area normalized Fe $L_{2,3}$ XAS (top) and XMCD (bottom) spectra as a function of TiN overlayer thickness. The XMCD intensity is corrected for incidence angle and incomplete degree of circular polarization of the beam.

The different binding energies for Fe in different valence states yield a method to differentiate the chemical state of the Fe. Iron in FeO is $Fe^{2+}$, iron in $Fe_2O_3$ is $Fe^{3+}$, and iron in $Fe_3O_4$ has a mixed valence. We can consequently determine the oxidation state of iron from the position of the Fe XAS L-edge, (lower binding energy for $Fe^{2+}$). Figure 2.4 shows the spectral weight of the $L_3$ edge shifting from the $Fe_3O_4$ position to the FeO position as the thickness of the TiN overlayer is increased from 0 to 48 Å. We conclude that there is a continuous decrease of $Fe_3O_4$ in the interfacial region via the formation of FeO. FeO is the by-product of oxygen out-diffusion from the $Fe_3O_4$ into the TiN (probably forming $TiO_2$). Although we were unable to directly monitor the formation of

$TiO_2$ from oxygen absorption at the TiN interface, the relative formation energies for various compounds strongly suggest $TiO_2$ formation as the most likely occurrence.

Overlayer Effects on $Fe_3O_4$: $SrTiO_3$ (STO)

STO has already demonstrated itself to be a high performance interlayer material for oxide bearing ferromagnets and was therefore considered as a candidate material[43, 44]. Figure 2.5 shows the peak area normalized Fe $L_{2,3}$ XAS and XMCD spectra as a function of STO coverage.

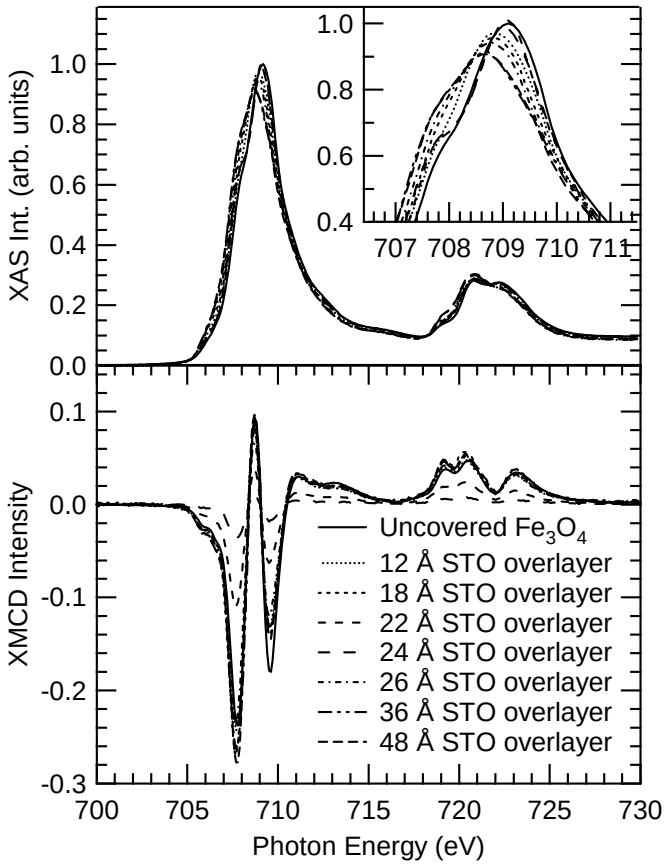


Figure 2.5. The peak area normalized Fe $L_{2,3}$ XAS (top) and XMCD (bottom) spectra as a function of STO overlayer thickness. The upper inset is an enlargement of the $L_3$ peak for detail. The XMCD intensity is corrected for incidence angle and incomplete degree of circular polarization of the beam.

Unlike the behavior from TiN overlayers, STO overlayers generate only minor changes in the XAS spectra and no change in the XMCD spectra (with two notable exceptions). For these two exceptions, (the 22 Å and 24 Å STO overlayer thickesses), we observe a substantially reduced XMCD intensity. The corresponding XAS spectra also exhibit a peculiar trend. Again for these thicknesses, the observed $L_3$ edge shift with increasing STO thickness is not a simple shift towards the FeO peak but rather a change in shape. Peak height at the initial position is in fact slightly increased and a clear shoulder appears on the left side of the $L_3$ edge. This can be easily observed in the enlarged inset to Figure 2.5. The reason for this XAS and XMCD behavior may be due to a magnetic reorientation, perhaps from a structural transition as the film thickness reaches approximately 22 Å. Additional work should be done to complement our preliminary results in this thickness range.

Additional insight into the overlayer effect on the $Fe_3O_4$ can be determined from the overlayer thickness dependence of the XMCD intensity, as displayed in Figure 2.6.

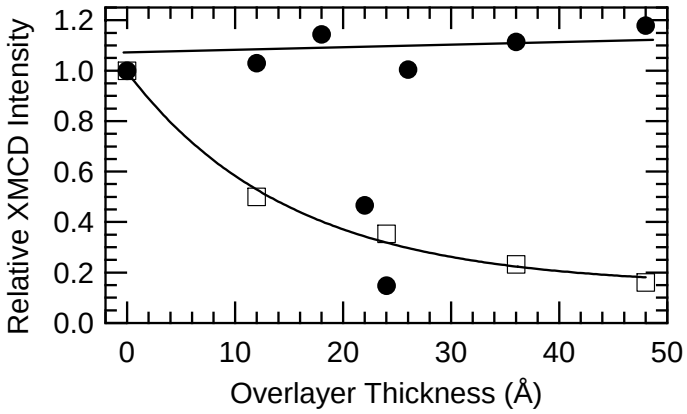


Figure 2.6. The Fe $L_3$ peak XMCD intensity for TiN (open squares) and STO (filled circles) as a function of overlayer thickness. The lines represents a least-squares fit through the data points for exponential (TiN) and linear (STO) fits.

For the TiN data, we see an exponential decrease of the $Fe_3O_4$ component with increased overlayer thickness. This type of decay is suggestive of a single dominant barrier to FeO formation. Furthermore, the XMCD intensity is only sensitive to the ferromagnetic iron and therefore a direct measure of it. The STO data shows a constant XMCD intensity (except for the two thicknesses previously discussed).

To confirm that the XMCD spectra are direct indicators of the percentage of $Fe_3O_4$ in the interfacial region, Figure 2.7 shows all XMCD spectra after normalization to the peak-to-peak intensity.

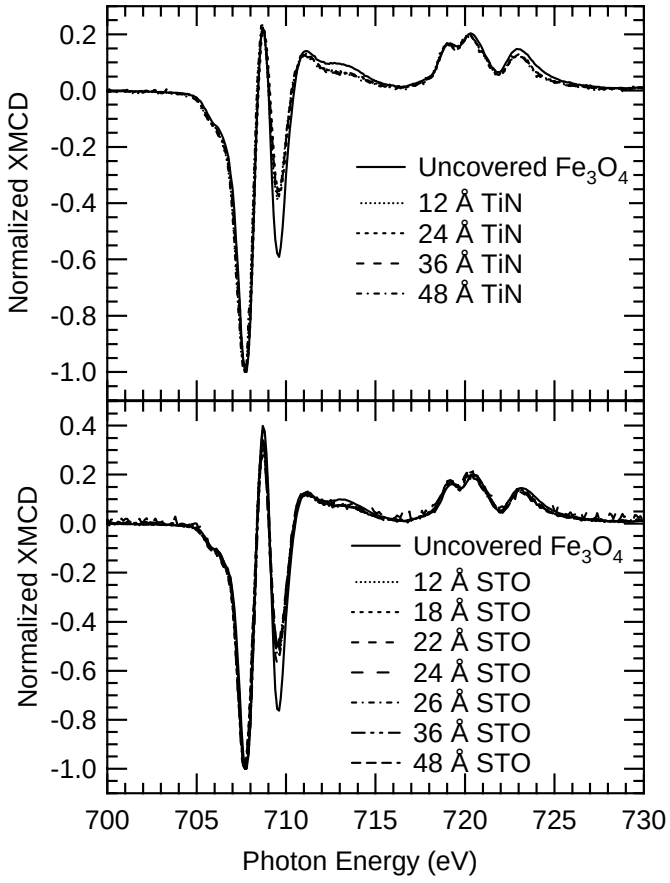


Figure 2.7. The Fe $L_{2,3}$ XMCD spectra all separately *normalized* to the first peak intensity for TiN (top panel) and $SrTiO_3$ (bottom panel) for all overlayer thicknesses.

In each case, all STO and TiN samples have exactly the same shape. There is a slight deviation when compared to the uncovered $Fe_3O_4$ films, but this may be due to a degradation of the uncapped films upon transport from the growth chambers, through extended periods of time in air, to the XMCD characterization chamber. It should be noted that the uncovered films used for comparison in the TiN and STO studies have slightly different XMCD spectra. This may represent growth variations from sample to sample, or these two uncovered samples may have experienced varying levels of exposure to air between growth and characterization, leading to slightly varying spectra. Note that for consistency, all samples in the two groupings (STO capping and TiN capping) were made together, but the two groups of samples were made months apart.

Still, we are confident that the Fe XMCD relative intensity is a direct measure of the percentage of $Fe_3O_4$ in the interfacial region. A further check of this conclusion can be made. By taking this percentage decrease in the XMCD intensity, (relative to the uncovered $Fe_3O_4$ XMCD intensity), we can determine the fraction of $Fe_3O_4$ lost due to oxygen out-diffusion attributed to the addition of the overlayer. Knowing this, we can scale the uncovered $Fe_3O_4$ XAS spectra by the determined percentage and subtract the reduced $Fe_3O_4$ contribution from the total measured XAS spectrum to obtain the residual spectrum representative of the nonmagnetic Fe component, (for identification purposes). Performing this procedure for all TiN overlayer thicknesses consistently yields the same spectrum, corresponding to the XAS spectrum for Fe in FeO. This procedure allows us to effectively quantify the FeO and $Fe_3O_4$ contributions of the XAS spectra and de-convolute them accordingly. The procedure and results are portrayed in Figure 2.8.

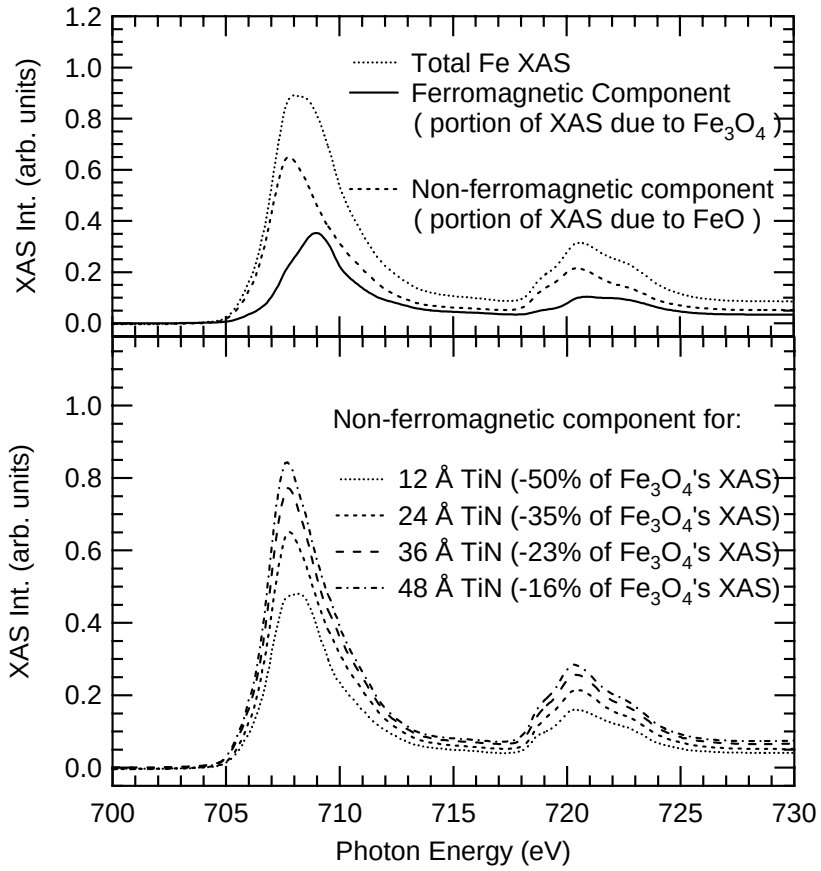


Figure 2.8. Top panel: The Fe $L_{2,3}$ XAS for the 12 Å TiN overlayer sample (dotted line), the scaled Fe $L_{2,3}$ XAS for the uncapped $Fe_3O_4$ (solid line), and the resulting spectra from the subtraction process (dashed line). Bottom Panel: Remaining component of the Fe $L_{2,3}$ XAS spectra for all TiN overlayer thicknesses after subtraction.

Finally, as a check, this same subtraction procedure can be applied to the two STO thicknesses that resulted in the greatly reduced Fe XMCD intensities (22 Å and 24 Å). This procedure, shown in Figure 2.9, results in two spectra which are very different from the FeO spectra of Figure 2.8, but similar to the $Fe_3O_4$ spectra. This is good evidence that the in this case, the reduction in XMCD intensity is not the result of $Fe_3O_4$ converting to FeO, but a change in the remnant magnetic state of the Fe. The chemical

state of the Fe is not altered by the STO overlayer, but a change in the magnetic state of the Fe may occur at a critical thickness of ~25 Å.

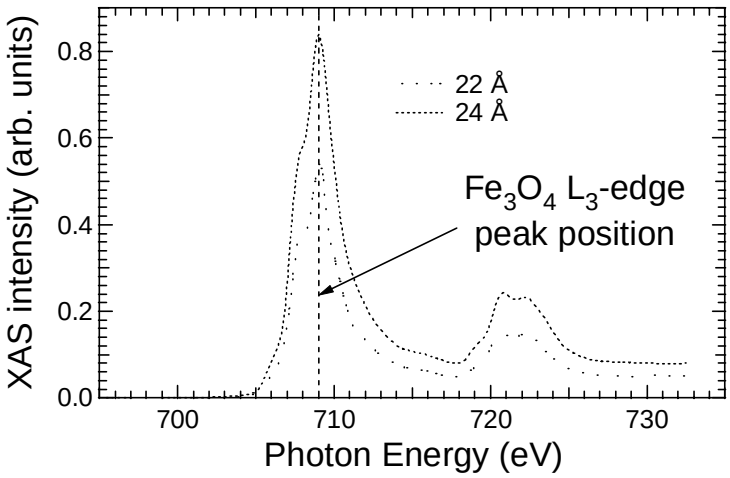


Figure 2.9. Remaining Fe $L_{2,3}$ XAS spectra for two STO overlayer thicknesses after subtraction process. The major peak is still aligned to the $Fe_3O_4$ peak position (dashed line).

Summary

The combined use of XAS and XMCD, in a qualitative and quantitative manner, allows us to conclude that the deposition of titanium nitride on $Fe_3O_4$ disrupts the interface via the formation of FeO, and the concurrent loss of magnetization, rendering it an unsuitable interlayer material for $Fe_3O_4$ based multilayer magneto-conductive devices. Our preliminary results on STO support the idea that it preserves the $Fe_3O_4$ film intact, thus proving to be a promising alternative for interlayer materials.

# MATERIAL CHARACTERIZATION

## Overview

As novel materials, the Dilute Magnetic Semiconductor Oxides (DMSO) materials required extensive characterization. The characterization by numerous research groups lead to conflicting reports, due mainly to differences in preparation techniques. Our characterization studies have proven useful to characterize specific samples prepared by Pulsed Laser Deposition (PLD) by our collaborators at the University of Maryland and also regarding general properties of DMSO materials.

## Introduction to Structural Characterization

The structural characterization is important because several material properties can be deduced from it. For example, $TiO_2$ can be found in a variety of structural phases and each has different electronic properties. Various techniques can help determine the structural state of a material. Some techniques, such as Scanning Tunneling Microscopy (STM) and Atomic Force Microscopy (AFM), accurately yield the surface structure. Reflection High Energy Electron Diffraction (RHEED) is also surface sensitive and can be used during the deposition of films to monitor the growth process. Bulk techniques allow us to determine the crystal structure, assuming the material is crystalline. Such techniques include X-Ray Diffraction (XRD) and Neutron Diffraction, which provide information about the long-range order of crystalline materials. Transmission Electron Microscopy (TEM) provides bulk information in cross sections, assuming no surface reconstruction occurs, but requires destruction of the sample.

X-ray absorption techniques are a non-destructive way to look at the bulk of a sample or film with high sensitivity to the chemical and structural local environment. EXAFS is especially sensitive to the structural environment and allows us to determine the local crystal structure by comparison with theoretical simulations or reference spectra. The XAS spectral shapes are also sensitive to the structural and chemical local environment of atoms and can help determine those characteristics with element specificity. By this, we mean that we can look specifically at the local environment of one chemical species. One limitation is that we obtain an average spectrum for all atoms of a particular atomic species in the probing volume. The only way to achieve spatial resolution is to use a highly intense source of light and a small spot size. Still the maximum resolution is on the order of microns. Also, in total electron yield, the probing depth is on the order of a few hundred angstroms. Nonetheless, this technique has the advantage of being element-specific, non-destructive, and provides local structural and chemical information of even buried and/or dilute atomic species of a sample. We used this technique successfully to address the crystal structure of oxide films deposited in various temperature and oxygen partial pressures to establish the substitutional nature of cobalt atoms in the $TiO_2$ (and $SnO_2$) matrix, and also to examine oxygen and oxygen vacancies.

## Structural Characterization of Co-doped $TiO_2$

### Introduction

When room temperature ferromagnetism was discovered, and subsequently confirmed in Co-doped $TiO_2$, it was for the anatase phase[12, 13, 15]. This is partly why most

groups interested in further investigating this material strive to obtain form of $TiO_2$. However, the anatase structure is thermodynamically unfavorable[45] and reverts to the more stable rutile structure at elevated temperatures[46]. Therefore, this study was useful in determining the effectiveness of substrate-induced stabilization of the anatase structure, (both structures are tetragonal but have different lattice parameters). It has since been shown that both the rutile and anatase phases are ferromagnetic at room temperature. Yet, the two structures lead to various properties. For example, in the undoped form, anatase has been shown to have a wider optical-absorption gap than rutile and a smaller electron effective mass presumably leading to higher charge carriers mobility[47]. These small differences can be essential in future applications. In fact, the different properties of rutile and anatase have been successfully utilized in the same device. For example, a typical low-cost photovoltaic module is composed of a transparent conducting photo-electrode of dye-sensitized nanocrystalline anatase, a spacer of electrically insulating, light-reflecting particles of rutile, and a counter-electrode of graphite powder[48]. Hence, anatase is used because of its efficient coupling with the dye, and rutile for its high dielectric constant.

For most spin transport electronics applications, these materials must be grown as thin films. As successfully demonstrated in other systems, it is possible to stabilize the anatase phase by growing it on an appropriate substrate. Two substrates were identified by the scientific community as good candidates to stabilize the anatase phase: $SrTiO_3(001)$ and $LaAlO_3(001)$[12, 45, 49, 50]. The lattice match between the cubic $SrTiO_3$ (a = 3.905 Å) and the tetragonal anatase $TiO_2$ (a = 3.784 Å, c = 9.515 Å) helps promote the growth of anatase with the c axis perpendicular to the film plane. The rutile structure of

$TiO_2$ is also a tetragonal crystal but with a poor lattice match (a = 4.585 Å, c = 2.953 Å)[51]. We performed X-ray Absorption Spectroscopy (XAS) measurements at the oxygen, titanium, and cobalt edges of Pulsed Laser Deposited (PLD) samples.

The Co-doped anatase is properly described by $Co_xTi_{1-x}O_{2-\delta}$, where the "δ" represents oxygen vacancies, which must exist to maintain local charge neutrality of the sample by compensating for the cobalt (valence 2+) substituted titanium (valence 4+) atoms. It is therefore not surprising that the sample's structure depends strongly on the oxygen partial pressure during growth. Recall also that that oxygen vacancies can generate polarons, which may be mediating ferromagnetism, and they generate charge carriers (electrons in this case) that make $TiO_2$ an n-type semiconductor[13]. Although there is debate over the exact mechanism for ferromagnetism, all agree that oxygen vacancies play a role.

Experimental

In this study, $Co_xTi_{1-x}O_{2-\delta}$ films (x = 1% and 7%) were pulsed laser deposited (PLD) on $SrTiO_3$ at various temperatures and in various partial pressures of oxygen ($PO_2$). Rutherford BackScattering (RBS), X-Ray Diffraction (XRD), and Vibrating Sample Magnetometry (VSM) measurements on some of the samples have been published elsewhere (see Shinde *et al.*[15]). The samples were shown to exhibit ferromagnetism at high temperatures and high temperature treatment was found to dramatically enhance Co incorporation in the matrix. Subsequent XAS results (our work) allowed us to determine the necessary conditions that enable the substrate-induced stabilization of the anatase structure. We used XAS to measure the $L_{2,3}$ edges of cobalt and titanium, and the K edge of oxygen.

Rutile and anatase $TiO_2$ have been studied extensively, making XAS intensity profiles of oxygen and titanium, in rutile or anatase, available for comparison with our spectra. Our spectra are in fair agreement with calculations by F. M. F. de Groot[52, 53] and in very good agreement with XAS spectra measured by Ruus *et al*.[54] and Soriano *et al*.[55]. By comparing our oxygen and titanium XAS spectra with previously measured spectra we can determine whether our Co-doped samples are in the anatase, rutile, or some other $TiO_2$ structure.

To make the structure identification, the revealing feature is a double peak in the Ti $L_{2,3}$ spectrum at around 460 eV. For the anatase structure, the left peak dominates, while for the rutile structure, the right peak is the larger of the two. Similarly, the oxygen spectral shapes reveal whether the probed oxygen is in an anatase or rutile structure. Having both oxygen and titanium spectra for comparison allows us to determine our sample's structure with confidence.

Substrate Temperature During Deposition

Titanium and oxygen XAS measurements on samples grown at various substrate temperatures (see Figure 3.1) reveal a lower limit to the temperature at which films can be stabilized in the anatase structure for Co-doped $TiO_2$. We find that for successful substrate-induced stabilization, the titanium, cobalt, and oxygen atoms must have a minimum mobility, allowing them to conform to the substrate. At low temperatures the reduced mobility causes the substrate-induced anatase structure growth to be compromised allowing the films to adopt the more thermodynamically stable rutile structure.

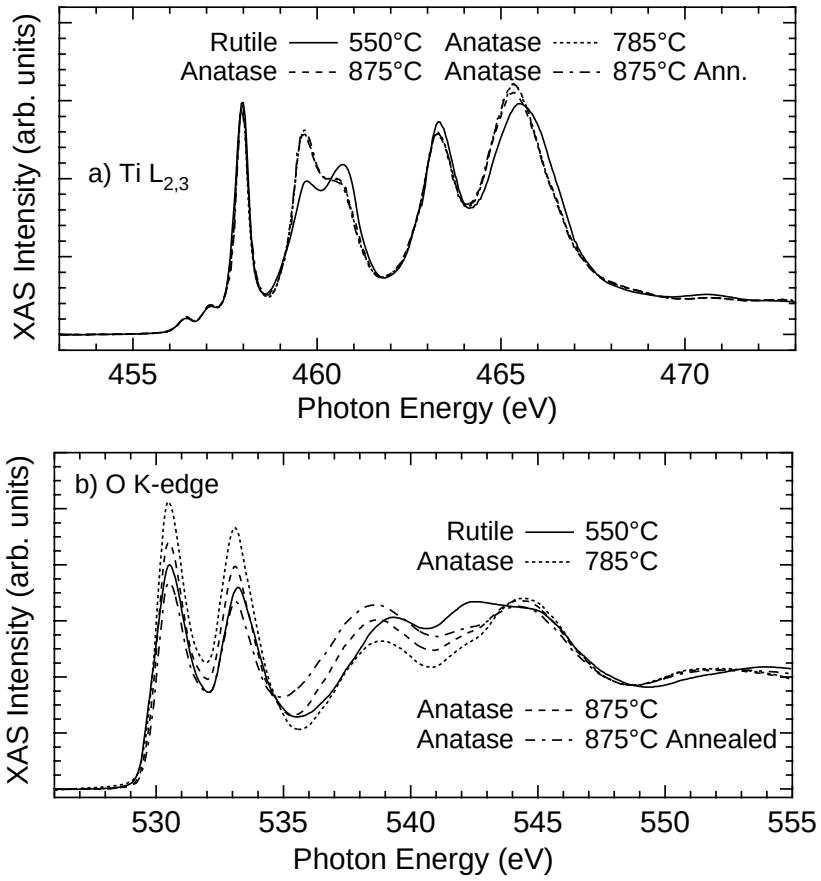


Figure 3.1. The titanium $L_{2,3}$ XAS (a) for 7% cobalt-doped $TiO_2$ films grown at various substrate temperatures. Only the lowest growth temperature yield the rutile structure while all others resulted in anatase. Annealing the sample results in no significant difference in the titanium spectra. The oxygen K edge spectra (b) confirm the titanium results. Spectra from all samples have the same general features except for that of the sample grown at 550°C, which is characteristic of the rutile structure.

Oxygen Partial Pressure During Deposition

The oxygen partial pressure ($PO_2$) dependence was determined for two sets of samples deposited at 700°C with 1% and 7% cobalt doping. We find that there is a minimum $PO_2$ required to obtain the anatase structure (see Figure 3.2). Indeed, below a certain $PO_2$ the films grow in the rutile structure, or at very low $PO_2$, they may adopt the so-called $TiO_2$-II structure. Although the $TiO_2$-II XAS spectral shape resembles a

mixture of anatase and rutile, this structure is an entirely different (orthorhombic) structure[54]. We understand the $PO_2$ effect by recognizing that oxygen has a lower sticking coefficient on a fully oxidized surface so titanium dictates film deposition kinetics and anatase growth must occur at an overpressure of oxygen (well above stoichiometric ratios).

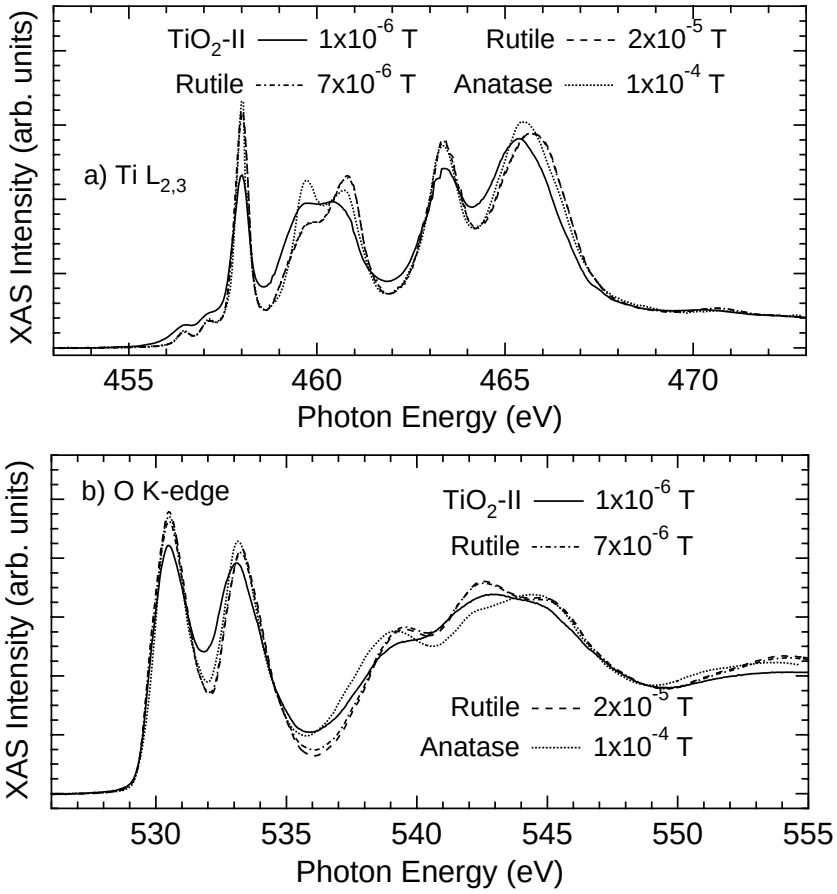


Figure 3.2. Titanium spectra (a) for 1% Co samples deposited in various $PO_2$, but all at 700°C. Oxygen partial pressures above 1 x $10^{-4}$ are necessary to ensure growth in the anatase structure. The oxygen spectra (b) for the same samples confirm the conclusions reached from the titanium spectra. For partial pressures below approximately 5 x $10^{-6}$ Torr we obtain a spectrum similar to that of the $CoTiO_2$-II structure.

Oxygen deficiency will again compromise the substrate-induced anatase structure stabilization. Interestingly, at the threshold oxygen partial pressure between the formation of anatase and rutile there appears to be a region of mixed phase. This was revealed by the sample grown at the threshold $PO_2$ of $2x10^{-5}$ Torr, for which the surface region is in the rutile structure while the bulk appears to be in the anatase structure (as revealed by XRD measurements by Shinde *et al.*[15]). The titanium spectra and oxygen spectra share the same general features whether samples are grown with 1% or 7% cobalt doping; therefore, so the 7% spectra were omitted in Figure 3.2. Conclusions we draw concerning $PO_2$ effects on growth are, by and large, independent of cobalt doping concentration.

Cobalt Spectra

The cobalt $L_{2,3}$ XAS spectra shown in Figure 3.3 are in agreement with those published by Chambers *et al.* for Co doped anatase $TiO_2$[13]. They very closely resemble $CoTiO_3$ spectra, providing evidence that cobalt atoms take on substitutional lattice sites, based on the spectra's sensitivity to the local structure[13]. In anatase and rutile $TiO_2$ or in $CoTiO_3$, cobalt atoms are thus expected to be octahedrally coordinated by 6 oxygen atoms in slightly different states of distortion. The spectral shapes display minimal change with varying growth conditions or resultant structure. Note the circled features above both the $L_2$ and $L_3$ edges in the Co spectra. As we will discuss later, these features are not specific to the rutile structure but indicative of low cobalt concentration in the probing volume.

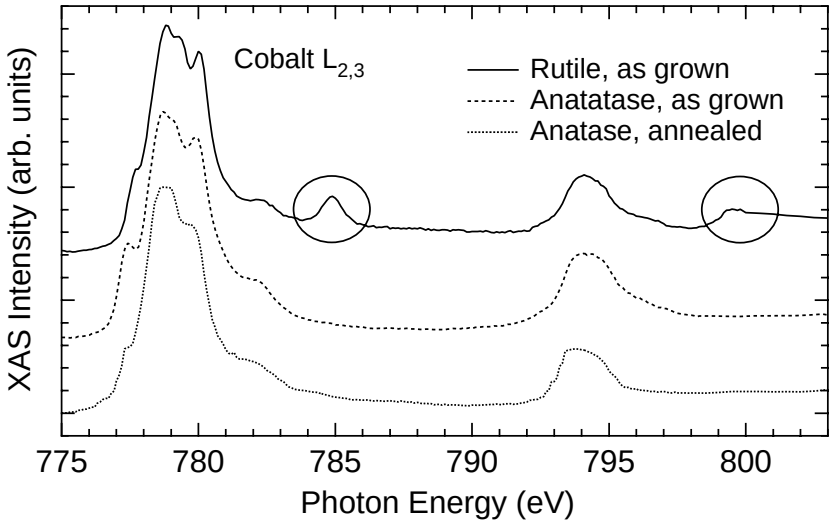


Figure 3.3. Cobalt $L_{2,3}$ spectra. Rutile and anatase samples (as determined from the oxygen and titanium spectra) have similar cobalt spectra. The additional circled features are a characteristic of low concentration samples The effect of annealing on the cobalt spectra of 7% Co-doped samples is also shown. The sharpening and partial loss of shoulder features suggests a partial transformation to metallic cobalt.

Also included in Figure 3.3 is the cobalt $L_{2,3}$ XAS spectrum for a sample that was post annealed in vacuum at 875°C in an attempt to create conductivity enhancing oxygen vacancies and to disperse clustered cobalt atoms in the film[18]. We remind the reader that although cobalt clusters in a semiconducting matrix exhibit macroscopic ferromagnetism, an intrinsic ferromagnetic semiconductor is necessary to achieve successful interfacing with traditional semiconductors. Cluster dispersal is therefore desirable. The present work shows that annealing also causes out-diffusion towards the surface. Other work shows clustering also occurs preferentially at the substrate interface[56] at low oxygen partial pressures. In any case, the consensus is that clusters form at film boundaries. Metallic clustering and its contribution to the spectra is substantiated by the sharpening and loss of shoulder features of the $L_3$ edge of the annealed spectrum in Figure 3.3, both suggesting a partial transformation to metallic cobalt. Because XAS is near-surface

sensitive, and previous work shows dispersal in the bulk[18], we conclude that some metallic clustering occurs near the surface. Our conclusions apply to our sample that was annealed in vacuum. Other studies show that annealing in an oxygen environment leads to similar results[14] and annealing in argon caused dispersal but no clustering[18].

This study allowed us to determine the suitable oxygen partial pressure and substrate temperature conditions that allow for substrate-induced stabilization of cobalt-doped anatase $TiO_2$ grown by PLD. The phase diagram shown in Figure 3.4 best describes our results. Deposition temperatures must be high enough to induce mobility of deposited atoms and epitaxial conformation to the substrate. A minimum $PO_2$ ensures enough oxygen is present during deposition, in spite of oxygen's higher volatility, compared to titanium and cobalt. Post-annealing leads to out-diffusion of cobalt and metallic surface clustering.

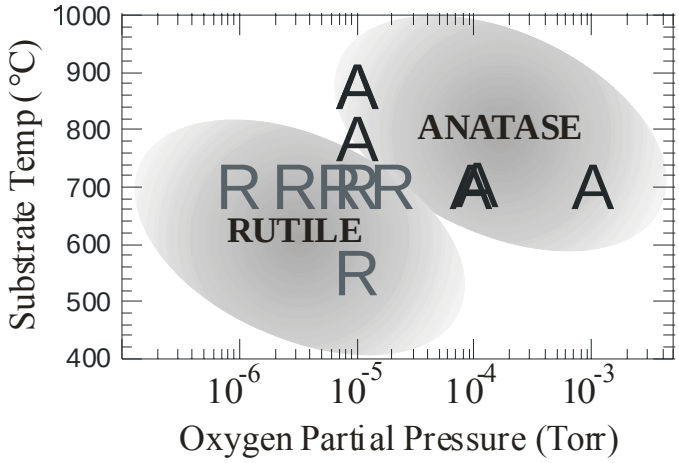


Figure 3.4. Phase diagram for partial oxygen pressure and substrate growth temperature requirements that allow for substrate-induced anatase structure stabilization on $SrTiO_3$.

Clustering at the boundaries from annealing, or in less than ideal deposition conditions, also confirms the limited solubility of cobalt in $TiO_2$, which is now accepted

to be at around 2%[15, 57]. This is not to say that higher concentrations cannot be achieved; however, they will not result in a stable material.

Film Thickness

Finally, we have evidence that the substrate-induced stabilization is effective up to a certain film thickness. For thick films, away from the substrate interface, the structure relaxes to its more stable rutile phase. While most samples were 1,500 Å to 2,000 Å thick films, certain samples were prepared as 8,000 Å films in order to obtain a better signal to noise ratio in the magnetic data. However, for those thick films XAS revealed the rutile structure. Recall that XAS is sensitive to the film's top few hundred Angstroms, but bulk sensitive XRD measurements by our collaborators revealed predominantly the anatase structure. Presumably, inevitable defects throughout the film compromise the continued epitaxial growth beyond a certain thickness.

## Substitutional Nature of Co in Co-doped $TiO_2$ (and $SnO_2$)

The substitutional (or interstitial) nature of cobalt atoms in the $TiO_2$ matrix is important because it has a strong influence on the valence state of cobalt atoms and how the doped cobalt atoms interact with the host matrix. We compared XAS measurements at the cobalt $L_{2,3}$ edge and the oxygen K edge of Co-doped $SnO_2$ and Co-doped $TiO_2$. The results show that cobalt atoms are in the same local environment in both compounds and help confirm that they occupy substitutional cation sites in the $TiO_2$ (or $SnO_2$) matrix, and that they are in the divalent oxidation state. Additionally, the oxygen spectral shapes offer insight into a possible cause for the observed giant magnetic moment of cobalt

atoms present in $SnO_2$[18], but not in $TiO_2$, thereby conveying the importance of the host oxide in the resulting magnetic behavior.

A Few Words on $SnO_2$

Undoped $SnO_2$ is considered "the" prototype transparent conductor[58]. It has high metallic conductivity and is optically transparent in the visible range. This makes $SnO_2$ (with its alloy with $In_2O_3$) technologically useful as a transparent electrical contact in such devices as flat-panel displays[59] and solar cells[60]. The conductivity has been explained theoretically in terms of high structural non-stoichiometry due to small defect formation energies of interstitial tin, and oxygen vacancies[58]. Previous experimental results on various dilute magnetic semiconductors, in particular Co-doped $TiO_2$, by other authors[37, 61, 62], have suggested that magnetic interactions in those materials are charge carrier mediated. In light of this, tin dioxide's relatively high carrier concentration made it a promising candidate as a magnetic semiconductor.

Experiment and Results

The $Co_xSn_{1-x}O_{2-\delta}$ samples were grown by pulsed laser ablation, with thicknesses of approximately 1500 angstroms on R-plane sapphire substrates. The cobalt doping levels were x = 5% and 8%, and $\delta$ stands for oxygen vacancies. More details on growth can be found elsewhere[18]. The $Co_{0.07}Ti_{0.93}O_{2-\delta}$ samples were grown by pulsed laser deposition with similar thicknesses on STO or LAO substrates. Again, additional sample growth details can be found elsewhere[15].

The cobalt XAS $L_{2,3}$ edge spectra for Co-doped $SnO_2$, are similar to those of cobalt in $TiO_2$ as shown in Figure 3.5. They share similar general features with only

slight differences in relative peak intensities. Strong similarities in the spectra can be seen from the weak difference observed between the $SnO_2$ and $TiO_2$ spectra (included on Figure 3.5). The similarity we observe in XAS spectral shapes is indicative of a similar local environment (structural and chemical) and oxidation state for cobalt atoms, regardless of whether they are doped in $TiO_2$ or $SnO_2$. These conclusions regarding the spectral shape are supported by recent independent experimental and theoretical work[63]. The cation substitutional sites in both compounds have the same distorted oxygen octahedral coordination[55, 64] suggesting that cobalt atoms sit at a substitutional site; in agreement with cobalt K-edge XAS of Co-doped $TiO_2$ samples by Chambers *et al.*[65]. Our L-edge spectra indicate that cobalt atoms are most likely substitutional in $SnO_2$ also.

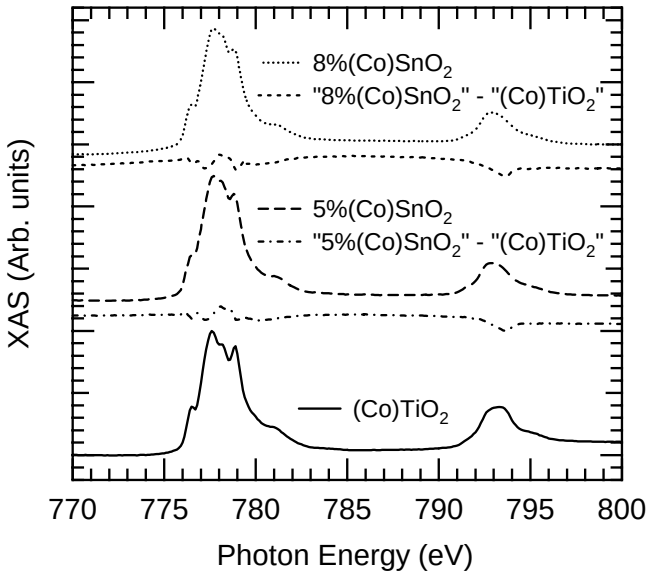


Figure 3.5. The XAS cobalt $L_{2,3}$ edge spectra for Co-doped $SnO_2$ and $TiO_2$. The great similarity in features offers evidence for cobalt atoms occupying oxygen octahedral coordinated cation sites in both compounds. Below the 5% and 8% curves are shown the difference curves, for which the anatase (7%) Co-doped $TiO_2$ spectrum has been subtracted.

A marked difference between $TiO_2$ and $SnO_2$ is that cobalt doped in $SnO_2$ can lead to giant magnetic moments. By this, we mean that if the magnetic moment of a Co-doped $SnO_2$ sample is completely attributed to the cobalt atoms in the sample, we have to assume that each cobalt atom has a magnetic moment of 4 to 6 Bohr magnetons[18] (this means that the magnetism is not carried exclusively by the cobalt atoms). Although the cobalt atoms have analogous nearest neighbor coordination in both compounds, we detect an important difference in their magnetic behavior. The oxygen spectra hint to a possible explanation.

For some time, the ferromagnetism in these dilute oxides has been generally accepted to be charge carrier mediated, although a specific mechanism is still lacking. The most promising polaron percolation model will be discussed in more detail later. Additionally, the charge carrier density is largely affected by oxygen vacancies[16], and therefore closely associated with oxygen. If the electronic states of oxygen in $TiO_2$ and $SnO_2$ (which are revealed in the XAS spectra) are significantly different, we might expect the magnetic properties of the compound to be different as well. As seen in Figure 3.6, even though the cobalt spectra are similar, the oxygen spectra are dramatically different.

Note that oxygen atoms in $TiO_2$ or $SnO_2$ have only about 5% of their cation neighbors replaced by cobalt. Concurringly, the XAS spectra of oxygen are virtually unaffected by the cobalt, and the obvious spectral differences reflect the different properties of the host lattice. The first peak at 530.5 eV in the $TiO_2$ oxygen spectrum represents the $t_{2g}$ band[52]. It is a sharp feature related to directional $\pi$-bonds and is completely suppressed in $SnO_2$. The bond directionality is conveyed by the comparison of spectra taken on a Co-doped $TiO_2$ sample with the photon incident beam normal to the

surface, or at 60° with respect to the sample normal. In this latter case the $t_{2g}$ feature is partly suppressed.

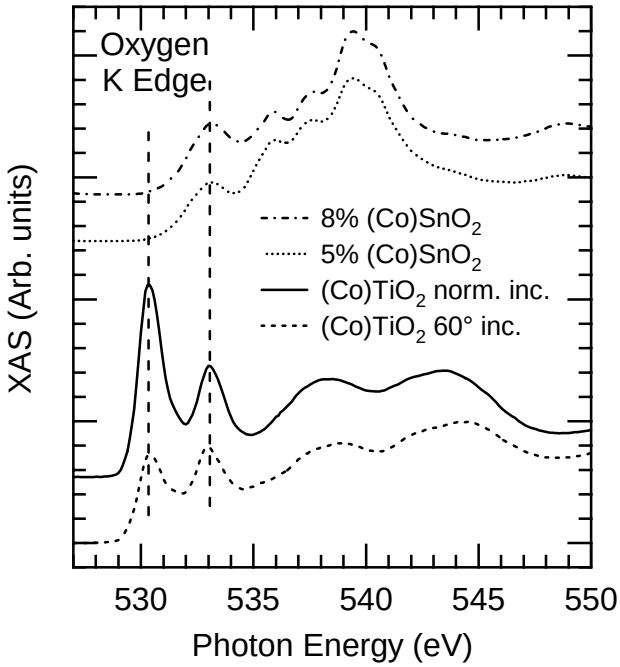


Figure 3.6. The XAS oxygen K edge spectra of Co-doped $SnO_2$ and $TiO_2$. The $t_{2g}$ band in the $SnO_2$ samples is completely suppressed. The $t_{2g}$ directionality is demonstrated by the feature suppression with changing photon incidence direction.

These distinctions indicate differences in the host oxide's electronic properties, which would in turn affect the carrier mediated magnetic interactions and possibly lead to giant cobalt magnetic moments in $SnO_2$. Amongst proposed explanations for the giant magnetic moment is un-quenching of the cobalt orbital moments[11], though it seems unlikely that un-quenching could be solely responsible for the observed moments. An alternative explanation lies in spin transfer on neighboring Sn atoms. XMCD, because of its element specificity, should be the ideal probe to explore this possibility; nevertheless,

attempts have been so far unsuccessful, as will be discussed later. Another as of yet uninvestigated possibility is that the magnetism could be related to oxygen vacancies (more on this later as well).

The giant magnetic moments in Co-doped $SnO_2$ are intriguing and we have observed an additional interesting time and history dependent behavior that is not present in its $TiO_2$ counterpart. In the graph below for example, we show how the saturation moment of Co-doped $SnO_2$ decreased after several measurements. This behavior, and additional considerations, have led us to believe that a spin-glass magnetic state occurs in this material. While making this system intriguing and scientifically interesting, it makes it less useful technologically. Nonetheless, the comparison with $TiO_2$ is useful to emphasize the role of the host matrix and, in particular, oxygen and oxygen vacancies in the observed ferromagnetism.

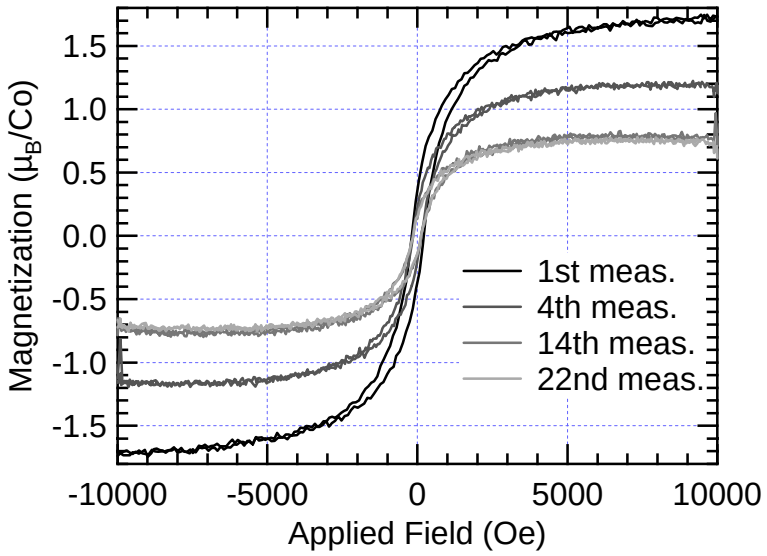


Figure 3.7. Several subsequent hysteresis measurements (M vs H) performed by Vibrating Sample Magnetometry (VSM) at 300 K showing the reduction of the saturation moment of a $Sn_{0.95}Co_{0.05}O_2$ thin film with field cycling.

## Magnetic Characterization

Considering we are trying to understand the magnetic interaction mechanisms for Co-doped $TiO_2$, one might expect that we dedicate more than one chapter section to the magnetic characterization. However, for the most part, the magnetic characterization is somewhat unexciting, and it has been accomplished by several other research groups. We know that the material behaves ferromagnetically. This is easily verified with Vibrating Sample Magnetometry (VSM) or Superconducting Quantum Interference Device (SQUID) measurements, which lead to S-shaped hysteresis loops with coercive fields that vary from 50 to 150 Oe, reaching saturation at about 5,000 Oe and with modest remnant magnetizations on the order of 6% of the saturation magnetization. In light of potential technological uses, this is less than ideal. We would hope to obtain squarer hysteresis loops. All the values quoted here relate to measurements performed at room temperature. By lowering the temperature we may obtain the desired square hysteresis loop behavior similar to the GaAs based Dilute Magnetic Semiconductor (DMS). This would not be futile because the oxide semiconductor based DMS have different interface compatibilities. However, the goal is, obviously, room temperature applications. Understanding the magnetic interaction mechanisms can be useful in eventually achieving the desired characteristics, which is why we pursue this work. For completeness, we include hysteresis loops measured by VSM. All measurements were done with the field applied in the film plane. Based on the film thicknesses, areas, and cobalt concentration, we were able to extract the magnetic moment per cobalt atom, expressed in units of Bohr magnetons.

Useful information can be extracted from the VSM measurements. First, the magnetic moment per cobalt atom calculation assumes that the total magnetic moment is due entirely to cobalt atoms. Clearly the magnetic behavior is not entirely attributable to scattered cobalt atoms that somehow couple ferromagnetically. One strong indication of this includes the failure to detect an XMCD signal at the cobalt L-edge, which is something we will address in the next section. Results we show in Figure 3.8 also demonstrate this fact by the lack of consistency, or even of an observable trend as a function of concentration, in the saturation moment per cobalt atom. Second, it's interesting to note the apparent lack of correlation between the hysteretic behavior and the film structure (anatase or rutile). In other words, the differing characteristics of anatase and rutile do not affect their respective magnetic behavior. Third, the film thickness does not affect the magnetic moment per cobalt atom.

In Figure 3.8, the last sample measured is listed as having 0% cobalt concentration. However, a cobalt XAS signal was measured on this sample so we conclude there was some contamination from previous depositions, though we do not know how much. We were able to deduce an approximate cobalt concentration of 0.5% ± 0.4% for this sample based on the relative size of the cobalt L edge and that of the titanium L edge. This is not an ideal way to deduce concentration because of the possible variability in cobalt distribution within the film and because XAS is sensitive to a limited depth. Also, because the absorption cross sections of the Ti L edge and the Co L edge are different, a simple ratio isn't appropriate. Nonetheless, we can consistently compare samples by this method. For all other films we use the nominal concentration, which was

shown by our collaborator to be fairly dependable by Rutherford Back Scattering (RBS) measurements.

We carried out measurements from -10,000 Oe to 10,000 Oe to ensure we achieved saturation but show only data -7,000 Oe to 7,000 Oe to allow better detail in the region of interest. All the hysteresis loops have a diamagnetic background contribution from the substrate subtracted to show the behavior of the Co-doped $TiO_2$ film only.

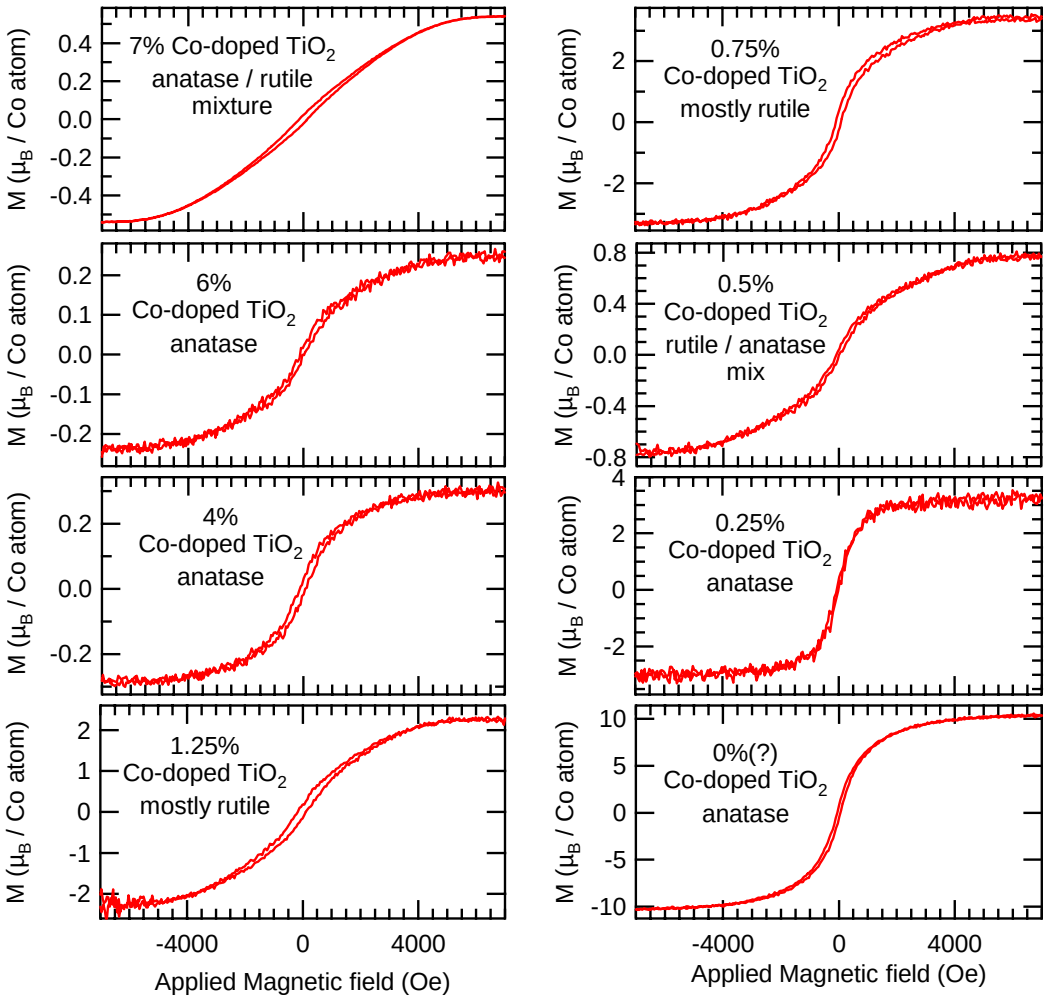


Figure 3.8. Hysteresis loops measured on various samples of Co-doped $TiO_2$ of various thicknesses. Please refer to the text for additional details and clarification on the measurements and data analysis.

Lack of XMCD

Regarding the magnetic properties of Co-doped $TiO_2$, or any of the currently studied magnetically doped oxides, there is one particularly interesting peculiarity. To this day, all research groups have failed to measure an XMCD signal in spite of samples being evidently ferromagnetic, as measured by other techniques.

XMCD effectively measures the imbalance in the up and down spin electrons associated with a chosen atomic species within a sample. This makes it a direct measurement of the origin of the macroscopically observable magnetic moments. The lack of XMCD is therefore extremely puzzling. For some time, the possibility that magnetism could be undetectable by XMCD had even never been considered. Incidentally, this is what led Kim *et al.* to mistakenly report that ferromagnetism in Co-doped anatase $TiO_2$ was due to exclusively to cobalt metal clusters. They didn't observe an XMCD signal until after they induced clustering (by annealing) and therefore assumed the samples were not ferromagnetic until they did. Additional VSM or SQUID measurements on the same samples, however, would have likely revealed the ferromagnetism in the unclustered samples as well.

Our combined XMCD and VSM measurements show that samples can have a ferromagnetic hysteresis loop without exhibiting an XMCD signal (see Figure 3.9) forcing us to look for explanations. Because we typically perform XMCD by pulsing an applied magnetic field and measuring absorption in the remnant magnetic state, the small remnant magnetization of Co-doped $TiO_2$ can difficult to detect. We repeated the experiments in an applied field (closer to saturation), but still observed no XMCD. Then, we have to face the possibility that the magnetic moment is carried by other atomic

species in the sample. We looked for an XMCD signal on the titanium and oxygen edges but could detect none.

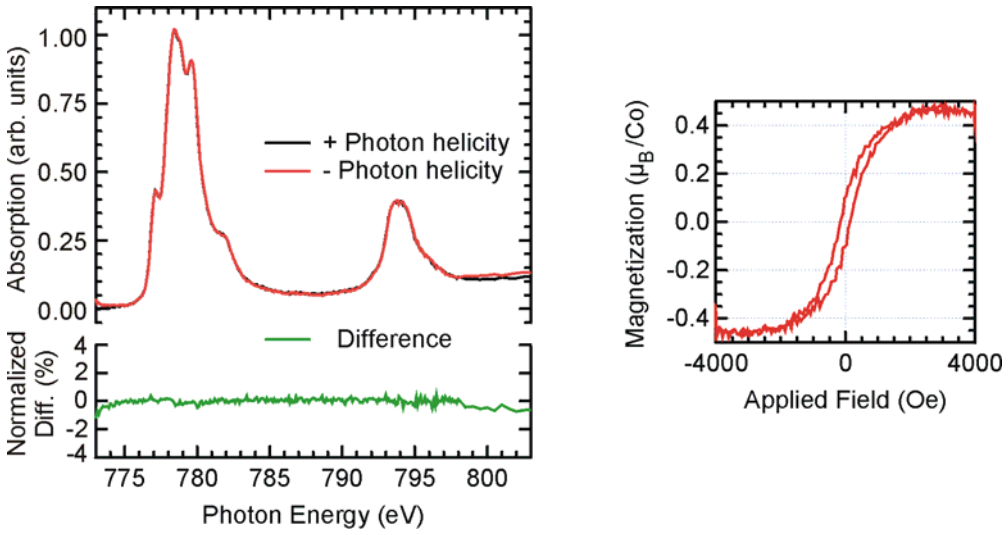


Figure 3.9. XMCD and VSM measurements on the same Co-doped $TiO_2$ sample clearly show the absence of XMCD in spite of the evident ferromagnetism observed by VSM.

Because at least one DMSO (Co-doped $SnO_2$) appears to possibly be a spin glass, with the associated unusual time dependent behavior, the idea that the magnetism could lag behind the magnetizing field was investigated. Since the typical XMCD procedure involves rapidly alternating the sample magnetization direction with applied magnetic field pulses, a time lag could have been relevant. The applied field pulses last a fraction of a second so a time lag of more than that, although extremely unlikely, would compromise the sample magnetization. The VSM measurements would not suffer from this possible time lag because the fields are ramped slowly and we would never notice a small time lag between the magnetization and the applied field. It is possible to perform XMCD measurements in an applied field, which we did, but still saw no XMCD signal. We also tried to study any possible long time scale magnetization processes explicitly by

monitoring the absorption intensity at the $L_3$ absorption edge, with polarized light and as a function of time, with or without an applied field. As it turns out the absorption intensity varies by up to 50% over a time period of minutes. This is much larger than what we could observe if the intensity variation was due to spin population imbalance. In other words, additional factors affect the absorbed intensity by such large values that we can never hope to detect the small variations that magnetization could be expected to induce. Our study was not in vain because it shows that large background artifacts can exist because of transient states by which samples either charge up, or heat up from exposure to X-rays. This leads to background absorptions that artificially vary in an exponential fashion. When this type of background is encountered in XAS or XMCD measurements. we can expose the sample to X-rays for a time on the order of minutes, until the background absorption stabilizes, to get rid of the large background variations that are difficult to deal with in subsequent data analysis.

Perhaps the most promising explanation for the lack of XMCD, though the details of how this may occur are uncertain, is that the magnetism (the spin imbalance) is carried on oxygen vacancy sites. Vacancies have no core electrons to excite to empty states above the Fermi level; therefore, no possible XAS or XMCD measurements can be performed on vacancies. Still, a vacancy is really an entity defined by its neighbors, in other words, a vacancy cannot exist without its neighbors and the electronic states that we associate with a vacancy are really connected to the neighbors. We thus have to wonder why an electronic imbalance on the vacancy site could not be detected from XMCD measurements performed on the vacancy's neighbors (the titanium atoms). A possible answer to this question is that only a small percentage of the titanium atoms (those with

an adjacent vacancy) would contribute to an XMCD signal; and this tiny signal would be difficult to detect on a large background signal contributed by the large majority of titanium atoms that exhibit no dichroism (those without adjacent, magnetic moment carrying vacancies). Typical XMCD differences are on the order of perhaps 5%. If 2% of the titanium atoms carry this 5% signal, we would then have to be capable of detecting differences in the $I^+$ and $I^-$ signals of 0.1%. For the dilute samples we are dealing with, the noise level is typically at least 1%. This is somewhat discouraging, but for the near future, finding ways to achieve better resolution may be the best way to look for a signal (although we cannot be sure it exists).

# POLARON PERCOLATION MODEL

## Previously Proposed Models

Cobalt-doped $TiO_2$ was discovered relatively recently[12] (2001). As we have seen, several issues pertaining to this material remain unresolved, including the mechanism that gives rise to ferromagnetism. For some time, only doped III-IV semiconductors were known to lead to ferromagnetism, and only at cryogenic temperatures. Accordingly, the first models of ferromagnetic exchange for dilute magnetic semiconductors were developed to explain ferromagnetism in those materials. Even for $Mn_xGa_{1-x}As$ the ferromagnetic interaction mechanism is still debated. For metallic systems weak carrier (hole) mediated coupling via the RKKY (Ruderman-Kittel-Kasuya-Yosida) interaction is expected to occur[66]. This long-range ferromagnetic interaction is in competition with the short-ranged antiferromagnetic direct exchange interaction between nearby Mn atoms. This causes the magnetic moment to increase with Mn concentration to a certain point, after which the short-ranged antiferromagnetic interaction wins over.

It is not surprising that this model was applied early to Co-doped $TiO_2$. One notable difference is that the interaction cannot be hole-mediated because $TiO_2$ is an n-type semiconductor with oxygen vacancies generating free electrons. Another problem includes the seemingly insufficient charge carrier density in some samples for the RKKY interaction to be effective. Furthermore, oscillatory nature of the RKKY interaction could lead to frustration and spin glass behavior for systems with short oscillation periods. Coey *et al*.[67] suggested the ferromagnetic interaction in Fe-doped $SnO_2$ could be due to F-center exchange, in which the interaction between two $Fe^{3+}$ atoms is mediated

by a common oxygen vacancy neighbor (see Figure 4.1[67]). However, this scheme requires iron atoms to be close to one another, which may not occur dependably in the case in dilute samples. Also, by Coey's own admission, the interaction energy is too low to account for the observed ferromagnetic behavior[68]. Later, new evidence showed that even insulating samples of Co-doped $TiO_2$ are ferromagnetic[34] and thus, the community was left to speculate regarding other mechanisms that could be responsible the observed ferromagnetism. Since then, the material has often been referred to as a ferromagnetic insulator. It can actually vary from insulating to semiconducting depending on the number of oxygen vacancies (which provide electrons and make the samples n-type semiconductors) present in the samples.

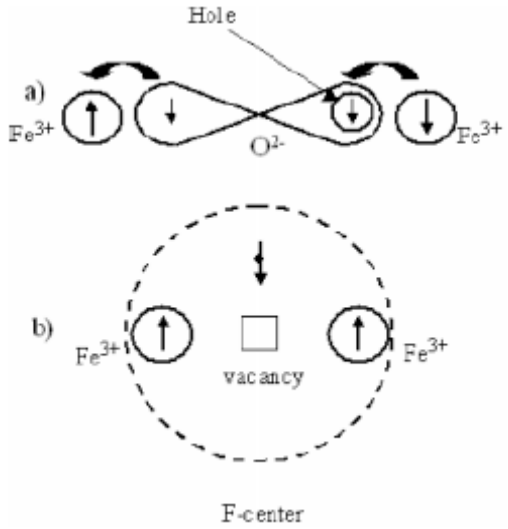


Figure 4.1. a) The superexchange interaction leads to antiferromagnetic coupling. b) The F-center exchange model as presented by Coey *et al*.[67]

## Polaron Percolation Model

The latest and apparently most promising theory that we discuss requires oxygen vacancies, or some other type of donor defects such as interstitial cations, but does not

require particularly high concentrations of such defects. The reason is that this theory is not based on an RKKY type interaction but on a polaron percolation model. Polaron theory was established some time ago[69, 70], but only fairly recently were polarons proposed to mediate ferromagnetic interactions in doped semiconductors. Kaminski and Das Sarma[31] developed the polaron percolation theory in 2002 for $Mn_xGa_{1-x}As$ and the theory was applied in 2005 specifically to magnetically doped oxides by Coey *et al.*[27]

The $TiO_2$ crystal, in the rutile or anatase form, is mostly ionic[71]. In the event of an oxygen vacancy, the electrons that would be given to the oxygen by the surrounding titanium atoms have no atom to call their own. They become loosely bound to the oxygen vacancy site in what can be considered (to first approximation) a hydrogen-like orbital. This constitutes a polaron. It is illustrated in Figure 4.2.

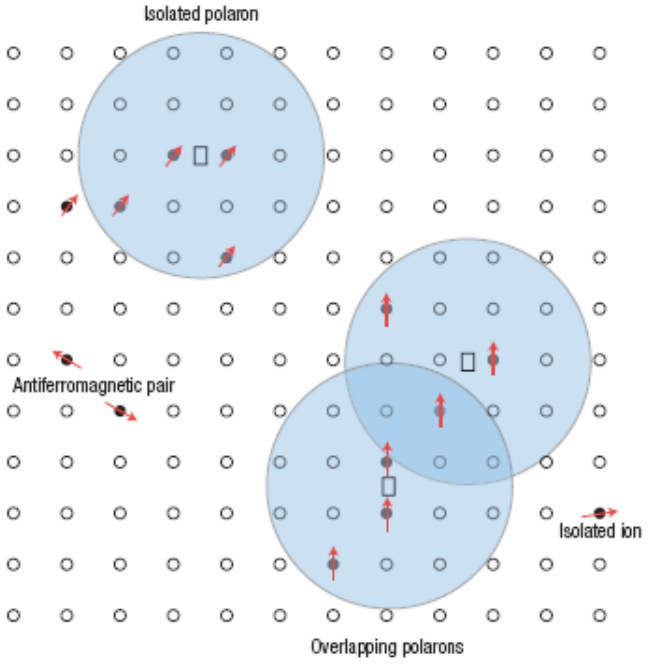


Figure 4.2. Polaron percolation model as illustrated by Coey *et al*.

The polaron can also result from an interstitial cation but in $TiO_2$ we expect that the main source of polarons will be oxygen vacancies. The complete interaction model is illustrated in Figure 4.2 and will be explained below.

This hydrogenic orbital radius can be large enough to encompass two or more substitutional cobalt atoms. According to the theory, magnetic impurity atoms can effectively couple with one another via their respective coupling to a single polaron. Depending on whether the cation 3d orbital is less than half full, or half full or more, the coupling with the polaronic electron is parallel or anti-parallel, respectively. Either way, by virtue of their coupling to the polaron, the cation impurities become effectively ferromagnetically coupled to each other[27]. The polaron radius is a function of the host material's dielectric constant and electron effective mass. If the polaron concentration in the material is large enough to achieve percolation, then an entire network of polarons and magnetic cations becomes interconnected and we observe macroscopic ferromagnetic behavior. Note that it may appear that a very large polaron concentration is required to achieve percolation but in fact only 16% *volume* fraction is required[72]. With large polarons this volume fraction may be achieved at relatively low polaron concentrations. With the extended radii of polarons, this concentration is not difficult to achieve without compromising the crystal structure's integrity.

Not only is this mechanism the most plausible put forward so far, but it also agrees with a model we deduced independently to explain the presence of a previously unreported and as far as we know, unobserved, spectral feature in the Co L-edge XAS of some Co-doped titanium oxides. The polaron percolation theory and our model complement and substantiate each other. This is precisely the topic of the next chapter.

# NON-PERCOLATING-POLARON MANIFESTATION IN XAS

## The L* Feature

As we investigated the cobalt-doped oxides by XAS we observed a new spectral feature that, to our knowledge, has never before been reported or observed. Having observed this feature for new and intriguing materials we have reason to believe that novel and interesting underlying physics could be at work. The feature is a sharp peak that appears approximately 6 eV beyond both the $L_2$ and $L_3$ edges of cobalt in XAS experiments. It is void of structure and reminiscent of a metallic cobalt L-edge, only shifted by 6 eV. We have labeled them the $L_3$* and $L_2$* features. They are observed above the $L_3$ and $L_2$ edges respectively.

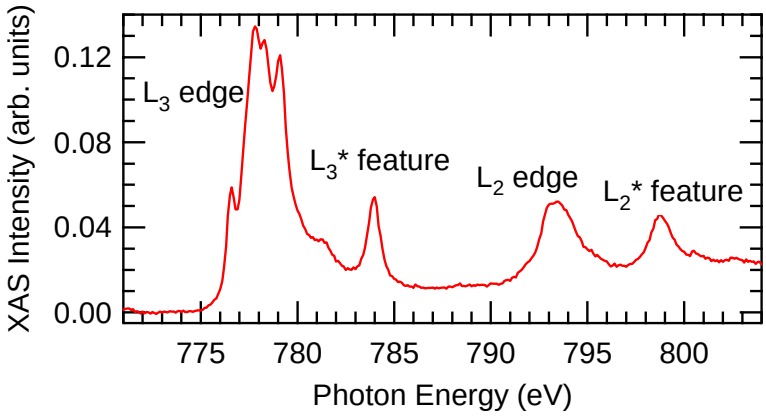


Figure 5.1. The L* features as observed for a pulse laser deposited thin film sample (1,500 Å) of 1.25% Co-doped anatase $TiO_2$ on an LAO substrate.

We have found that the L* feature is more than a small additional spectral feature. Its relative size is inversely related to the cobalt doping concentration and in samples doped with trace quantities of cobalt the L edge becomes imperceptible and the L* feature dominates the spectra. As the cobalt concentration increases in $TiO_2$, the L*

feature intensity decreases and finally vanishes at concentrations of just a few percent. This spectral feature has never before been observed for cobalt in any environment; prompting us to believe a specific characteristic of the doped oxides must be at the origin of it.

Occurrences of the L* Feature

So far, we have observed the feature in $TiO_2$ in both the anatase and rutile form, as well as in cobalt-doped $La_{0.5}Sr_{0.5}TiO_3$. The fact that we have observed the feature only in titanium oxides (so far) suggests that titanium may be important in explaining the feature. Nevertheless, we have no reason to believe the feature cannot exist in other systems. To answer an obvious question, we have verified that the L* feature is not a titanium absorption edge or a second order photon absorption of a titanium edge.

Intensity of the L* Feature

The L* feature's intensity appears to be affected by two factors. First, as previously mentioned, it is inversely related to the cobalt concentration. This has been verified for Co-doped anatase and rutile $TiO_2$. In Figure 5.2 we have plotted the XAS spectra of cobalt in anatase Co-doped $TiO_2$. The spectra have been area normalized. We quantify the feature's intensity by its fraction of the total spectral intensity. Mathematically, this means the L* intensity (or L* spectral component) is equal to the sum of the $L_3$* and $L_2$* peak areas divided by the sum of the $L_3$, $L_3$*, $L_2$, and $L_2$* peak areas. The results are plotted as a function of the cobalt concentration and exhibit a clear and interesting trend (see Figure 5.3). Second, the intensity is directly related to the oxygen partial pressure during preparation of the PLD samples (see Figure 5.4). The

surprising behavior of the L* feature's intensity with concentration and oxygen partial pressure can be understood with a model we developed.

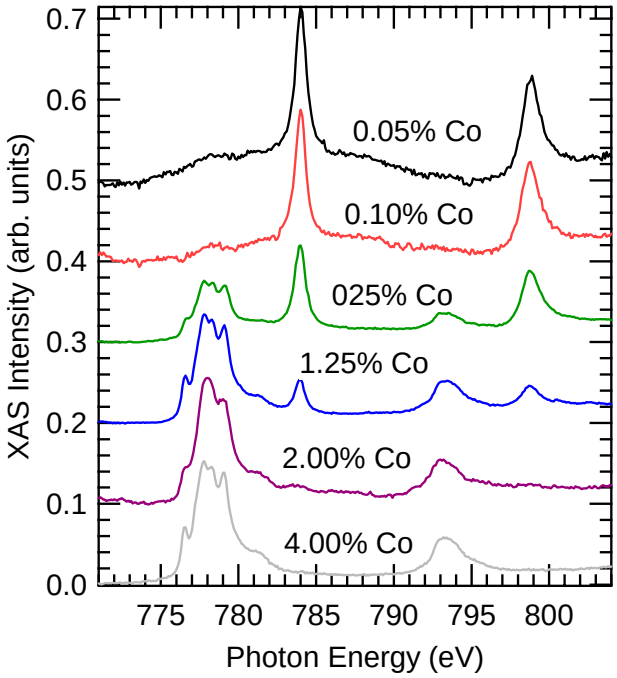


Figure 5.2. Cobalt $L_{2,3}$ edge XAS spectra of cobalt-doped anatase $TiO_2$. The spectra are offset and normalized such that we can visually track the spectral weight shift in the spectra.

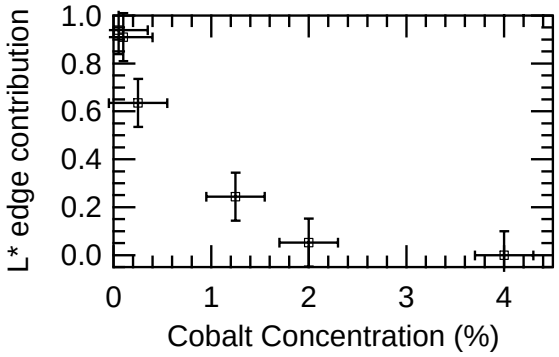


Figure 5.3. L* spectral component as a function of cobalt concentration for various sample concentrations of Co-doped $TiO_2$.

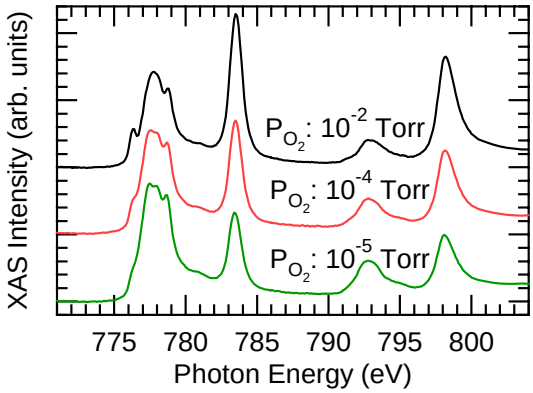


Figure 5.4. Cobalt $L_{2,3}$ edge XAS for thin films of cobalt-doped $La_{0.5}Sr_{0.5}TiO_3$ deposited in a range of oxygen partial pressures. Here, the spectra are offset and normalized such that the $L_3$ edge has an arbitrary intensity of 1.

In light of the dominant nature of the L* feature at very low cobalt concentrations (see Figure 5.2) it is clear that it is more than an *additional* feature, it is in fact an energy shifted absorption edge. The spectra are the result of cobalt atoms in two chemically and structurally distinct environments, some of which absorb at the conventional L edge, and others that absorb at the L* feature. This causes us to refer to the latter as the L* feature or the L* edge interchangeably.

## Isolated Defect Model

### Defect Model Description

The feature intensity behavior can be understood if we attribute the L* feature to isolated cobalt atoms. In the most general way, we can assign an *effective* diameter to all cobalt atoms and consider them isolated if no other cobalt atom resides within one diameter. Later, we will justify and quantify this *effective* cobalt radius. For now, we point out that it is reasonable to assume that cobalt atoms have a larger interaction radius than their physical atomic radius because, after all, they interact with each other in the

host lattice even thought they may be several sites away. If this were not the case there could be no ferromagnetism.

Given an effective defect radius, it is relatively straightforward to determine the proportion of defects (yet to be precisely defined) that are isolated from all others, as a function of defect concentration. We carried out Monte Carlo simulations in which we randomly positioned defects in a 50x50x50 cubic lattice, with periodic boundary conditions and then computed the fraction of isolated defects.

Following is a brief description of the simulation details. Each lattice site can be identified with three indices representing the x, y, and z positions. The main sub-routine requires the input of a defect concentration and radius. Based on the concentration, the appropriate number of defects (N) is determined for our 125,000 lattice sites model. The lattice indices of these defects (occupied sites) are determined by a random number generator and put in an Nx3 matrix. A variable is created to keep track of the number of isolated defects. We begin with the assumption that this number is zero (no isolated defects). Next, we run through a structure of imbedded loops that checks the isolated status of each occupied site. Each occupied site is assumed to be isolated until another is found within two defect radii of it. This effectively assumes that the defects are hard spheres (they overlap or they do not, but the overlap is not quantified). A condition is included at the beginning of the loop to avoid checking *all* sites if one has already been determined to be within 2 defect radii. At the end of the loop, if the status of a given occupied site has remained “isolated”, the number of isolated defects is incremented by 1.

For the simulations, the defect radius is expressed in units of lattice site separation, making the simulation generic to all systems. In order to apply the results to a

real crystal lattice we simply need to multiply the defect radius by the average inter-site separation in the real lattice. For example, in Co-doped $TiO_2$ the defects are cobalt atoms and they substitute for Ti atoms. Accordingly, the appropriate inter-site distance is the average distance between Ti lattice sites and is equal to 3.3 Å. It is important to point out that our simulations are based on a cubic structure although most physical crystal lattices are not. The reader should be cautioned that for small defect radii (on the order of an inter-site spacing) and large defect concentrations, this discrepancy could lead to errors. However, in the low concentration and relatively large defect regime the resulting error is negligible.

The main sub-routine described above is then imbedded into a larger routine that performs this calculation for a range of defect concentrations and radii. We suspect we could reduce computation time significantly by abandoning the "incrementation of the number of isolated defects" scheme and implementing a fourth column in the occupied-site-indices matrix which would contain the status of site (isolated or not). Then, when an occupied lattice site "B" is found within two defect radii of site "A", *both* sites would be deemed "not isolated" and there would be no need to check the status of site "B". Nonetheless, the simulations presented are correct and the relatively small simulation matrix we chose requires only an hour or two of computation time.

The simulation results are plotted in Figure 5.5. They are exciting for two reasons. First they reproduce the functional trend followed by the L* spectral component as a function of cobalt concentration remarkably well. This provides at least some validation of our claim that the defect feature is a characteristic of isolated cobalt atoms. Second, by matching the appropriate curve with the L* spectral component data, we

obtain an estimate of the defect's effective size. In Figure 5.6 we overlaid the "L* component versus concentration" data and all the simulation results to extract the correct effective defect radius. It is easy to see that the data is best matched by the simulation carried out with 5.9 Å radius defects (1.8 lattice-site-spacings).

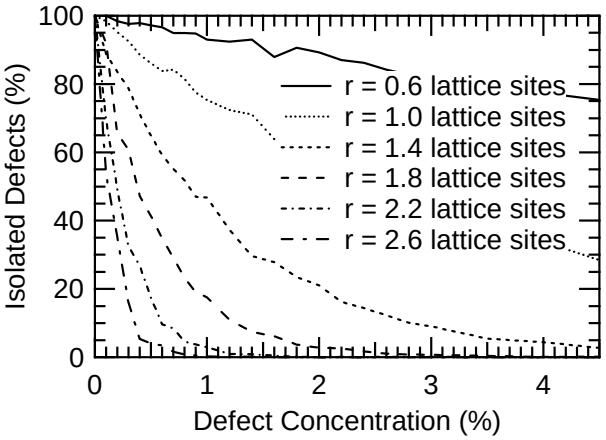


Figure 5.5 Monte Carlo simulations results showing the fraction of isolated defects as a function of defect concentration (%) for a range of defect radii. The defect radii are expressed in units of one inter-site distance.

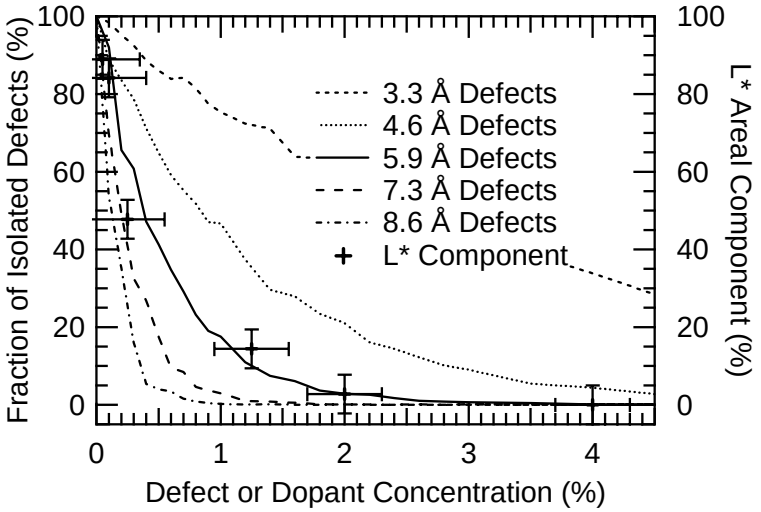


Figure 5.6. Combined Monte Carlo simulation results (left axis) and the L* spectral component as a function of cobalt concentration (right axis).

Origin and Significance of the Effective Defect Radius

We immediately recognized the role of oxygen and oxygen vacancies in the manifestation of the L* feature because of the oxygen partial pressure dependence of the cobalt-doped $La_{0.5}Sr_{0.5}TiO_3$. Preparing samples in lower oxygen partial pressures introduces additional oxygen vacancies in the samples. We believe that oxygen vacancies are an integral part of the defect. Increasing the vacancy concentration can be viewed as increasing the defects' effective radii, the defect concentration, or simply as increasing the abundance of the percolating phase that mediates the Co-Co interaction. In any case, a lower oxygen partial pressure will lead to more oxygen vacancies, fewer isolated defects, and a suppressed L* spectral feature, which is what we observe. This point of view is in direct agreement with polaron percolation theory. Oxygen vacancies, because they can result in polarons, can mediate the Co-Co interactions. Therefore, they have an important influence on the interacting or isolated state of cobalt atoms.

Polaron / Defect Size Considerations

As mentioned previously, from our data and simulations fit we extracted an effective defect radius of 5.9 Å. We have also established that oxygen vacancies (which constitute polarons) are an integral part of the defect. Cobalt atoms have a physical radius of only a few Angstroms, but the polarons are typically much larger. We therefore expect the polaron size to be the determining size scale for the cobalt/polaron defect. We will now show that the polaron size is equal to the defect size that we deduced from our fitting of the L* feature intensity.

The polaron radius can be determined using the following relation[69]:

$$r_H = \varepsilon_p (\frac{m}{m*}) a_0 \tag{5.1}$$

where $a_0$ is the Bohr radius, $m$ and $m*$ are the electronic mass, and effective mass, respectively. The *H* subscript stands for "hydrogenic" because the polaronic electron sits in a hydrogen-like orbital around its center.

The appropriate dielectric constant to use in determining the polaron ratio is given by the following relation[69]:

$$\frac{1}{\varepsilon_p} = \frac{1}{\varepsilon_\infty} - \frac{1}{\varepsilon_s} \tag{5.2}$$

where $\varepsilon_p$ is the appropriate dielectric constant required to calculate the polaron radius, $\varepsilon_\infty$ is the high frequency dielectric constant, and $\varepsilon_s$ is the static dielectric constant. The static dielectric constant is often much larger than its high frequency counter part. Consequently, the latter is sometimes used in the place of $\varepsilon_p$.

For anatase $TiO_2$ the dielectric constant and mass ratio (m*/m) are equal to 9 and 1, respectively. This yields a hydrogenic radius of 4.8 Å. Keep in mind that for such a hydrogen-like orbital the electron probability function decays exponentially with a characteristic radius of 4.8 Å but the actual range of the orbital extends to infinity. Mathematically, two hydrogenic orbitals always "touch" each other no matter what their separation. Physically, however, there must be a cut-off distance at which the orbital overlap is sufficient to declare the orbitals as "touching" and beyond which they do not effectively touch. In other words, there exists an appropriate hard-sphere approximation to this problem of interacting or non-interacting orbitals.

Figure 5.7 shows the orbital overlap, as a function of orbital separation, for hydrogenic orbitals with a characteristic radius of 4.8 Å. To calculate the orbital overlap, we integrate the product of two hydrogenic orbitals centered at *(-d/2, 0, 0)* and *(d/2, 0, 0)*, where *d* is the orbital separation. We perform the integration over all space. The interaction strength between orbitals is expected to be a function of the overlap squared. This curve is also plotted in Figure 5.7. For reference, the 5.9 Å hard-sphere cut-off is marked with a dotted line.

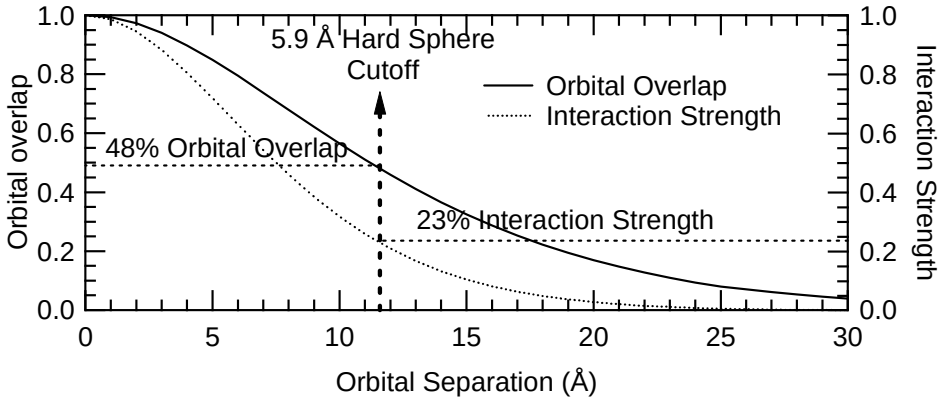


Figure 5.7. Calculated orbital overlap for hydrogen-like orbitals with a characteristic radius of 4.8 Å. The dotted line shows how approximating the 4.8 Å hydrogenic orbitals with 5.9 Å hard sphere orbitals is equivalent to considering less than 48% orbital overlap as non-interacting. Alternatively, it is equivalent to 23% interaction strength, which should scale as the overlap squared.

By drawing a horizontal from where this vertical line crosses the two curves of interest we can determine what approximating hydrogenic orbitals with 5.9 Å hard spheres means, quantitatively. It means that using 5.9 Å hard-spheres is the same as considering 48% or more overlap (23% or more interaction strength) as "interacting". In light of this analysis, 5.9 Å hard-spheres are a reasonable approximation of 4.8 Å hydrogenic orbitals.

This provides additional confidence that the defects (as deduced from our observations and simulations) are indeed related to the polarons postulated to mediate ferromagnetism in the semiconducting and insulating oxides.

## Origin of L* Feature

Ultimately, we strive to explain the exact mechanism leading to the L* feature. This is important not only for the sake of understanding this fascinating spectral feature but also because of its apparent connection to ferromagnetism in the dilute magnetic oxides. The definitive answer, and one that will be accepted by the research community, is not likely to emerge from experimental work exclusively. With appropriate theoretical confirmation we may settle this question once and for all. However, the theoretical work is difficult and requires extensive experience in theoretically calculating XAS spectral shapes. Our challenge has become to generate enough experimental evidence and a credible model to convince theoreticians to sacrifice time and effort into this problem.

### Possible Processes

It is pertinent to take time to examine the possibilities regarding the L* feature's precise origin. The conventional process leading to spectral features in XAS is the straightforward promotion of core-level electrons to empty states above the Fermi level. This is simply the resonant absorption of X-rays. We reiterate that the exact shape of the spectra is affected by initial and final states, which are themselves affected by the absorption process, but the general idea is that the L edge arises when 2p core electrons absorb photons and are promoted to empty electronic states above the Fermi level. The simple obvious assumption is that an additional empty state appears above the Fermi

level for isolated cobalt atoms in titanium oxides, and that electrons make transitions to this new state. This would indeed be surprising and no band structure calculations to date have revealed such a dramatic feature in the band structure.

We have also considered the possibility that the L* feature is not a conventional absorption edge but an *additional* spectral feature due to an excitation occurring in the material along with the conventional L edge absorption. Excitations such as a charge transfers, excitons, or phonons readily come to mind. Exciton energies are typically slightly less than the band gap (3.6 eV for anatase $TiO_2$) and phonon energies are on the order of meVs. Because the L* feature occurs roughly 6 eV above the standard L edges we could not attribute it to one of those processes (occurring along with a standard L edge absorption). Energetically, charge transfer events of 6 eV are possible. However, in light of our more recent measurements that reveal the L* feature only, (in the absence of the L edge), we had to rule out "*additional* excitation" processes altogether. In this recent data taken on very low concentration samples, it is clear that the X-ray absorptions at 784 eV and 799 eV (L* features) occur *instead* of the conventional L edge absorption. The L* feature cannot be considered an additional excitation feature. In samples for which both the L edge and the L* features appear, we must conclude that cobalt atoms in two different configurations are absorbing photons at different energies. Again, this reinforces the idea that the feature is characteristic of one type of cobalt atoms, namely the isolated cobalt atoms which absorb photons by a different process that requires approximately 6 eV more of energy. Such a large shift of the absorption edge (of the order of 6 eV) is surprising yet our observations force us to accept this position.

There are different ways by which the absorption edge can move up or down in energy (and shape). One possibility includes the cobalt 3d states, to which the transitions occur, being pushed up in energy. The hybridization with adjacent 1s polaron states may cause this but we have no theoretical evidence that this might be happening. In any case, a certain modification of the band structure does occur because the absorption edge is not only shifted but its shape is also changed. Namely, the L* feature lacks the fine structure seen in the conventional L edge. It may be that the edge shift is assisted by an increase of the 2p level binding energies. We know that cobalt substitutes for $Ti^{4+}$, creating an incentive for cobalt to be oxidized more severely than its typical 2+ valence state. Additional oxidation leads to less electronic shielding of the nucleus and higher binding energies. We confirmed, in chapter 3 that our XAS measurements show that cobalt atoms are in the +2 oxidation state. This, however, was for samples for which the L* feature does not appear. The L* feature, we now claim, is due to other cobalt atoms that are absorbing photons at higher photon energies and with a different spectral shape. It's possible that these cobalt atoms have a higher oxidation state. Two surprising observations remain unaddressed by this explanation. First, why is the absorption shifted by such a large (6 eV) amount? Typical variations due to valence differences are shifts on the order of 1 or 2 eV and/or spectral line shape changes, not 6 eV shifts. Second, this hypothesis offers no explanation for why the absorption edge's fine structure should disappear. The second point is actually not too surprising. Although the lack of fine structure is typically characteristic of the metallic state, cobalt in $La_{1-x}Sr_xCoO_3$ yields an L edge without fine structure[73]. Additionally, to address this and the previous question, we point to the unique nature and state of the isolated substitutional cobalt atoms, which

have never been studied previously. In the polaron percolation framework, s-d coupling occurs between the polaron and cobalt d orbitals. The p to s transitions are allowed by the selection rules so it may be possible for electrons undergo transitions from cobalt 2p core-levels directly to an empty substitutional-cobalt-d/polaron-s state. The situation we face is very unique and it may indeed explain the uniqueness of the observed L* feature.

Regarding theoretical calculations, in light of our recent results, for the cobalt atoms to be isolated sufficiently for all of them to absorb at the L* edge position their concentration must be on the order of 0.1%. No calculations have been performed at such low concentrations. None are likely to be done either because they would require a very large cluster size and unrealistically large computation time. Remember that 0.1% substitution means one cobalt atom per 1000 titanium atoms. One cannot simulate a fraction of an atom so the calculation requires the simulation of a cluster containing one cobalt atom and 999 titanium atoms (plus 2000 oxygen atoms). Typical calculations are done on clusters of tens of atoms. Additionally, $TiO_2$ is a strongly correlated system for which the creation of a core hole by photon absorption severely disrupts the local density of states. Therefore, we do not expect the X-ray absorption spectra to mirror the band structure. Accordingly, the theoretical XAS determination requires multiplet calculations, which are difficult, and to our knowledge, have yet to be performed even on less dilute systems. Unfortunately, this quells our hope of seeing computations confirm our hypotheses.

In the end, our experimental observations can only take us so far but they have significantly narrowed the possibilities. We hope they eventually lead to a complete understanding.

Substitutional Cobalt and Oxygen Vacancies

To fully justify the L* spectral component behavior and its association to cobalt atoms and related polarons we must remind the reader that there is a correlation between the concentration of substitutional cobalt atoms and that of oxygen vacancies (source of polarons). Our results presented in chapter 3 confirm that cobalt in Co-doped $TiO_2$ is in the divalent state (except possibly at very low cobalt concentrations) and substitutes for quadrivalent titanium atoms. This causes a local disturbance that entices the formation of oxygen vacancies in the immediate vicinity of the cobalt atoms in order to maintain charge neutrality. This view is agreed upon by all authors[15, 37] and suggests that oxygen vacancies are not only correlated to substitutional cobalt atoms but that they are also in the vicinity of these atoms.

For completeness, we must mention that not all oxygen vacancies constitute polarons. This is a point that has been largely neglected or overlooked in the literature so far. To discuss this issue, it is useful to introduce the notation in which $Co_{Ti}^{2+}$ stands for Co (2+) on a Ti (4+) site with an effective charge of +2, and vacancies are represented by the letter V. Several possible lattice responses will be discussed and illustrated in Figure 5.8. Notice that the lattice representations are symbolic and two-dimensional but convey the fact that each titanium atoms gives four of its electrons to four oxygen atoms. The idea that each $Co_{Ti}^{2+}$ is automatically and perfectly compensated by $V_O^{2-}$ is somewhat naïve and geometrically improbable (see Figure 5.8a). In $TiO_2$, titanium/oxygen bonds in $TiO_2$ are primarily ionic, but slightly covalent[71]. Each titanium atom "gives" four electrons to oxygen neighbors and each oxygen atom "takes" two electrons from titanium neighbors but the covalent character causes them to "share" electrons. Moreover, each

oxygen atom pulls two electrons from two *different* titanium atoms, so from geometrical considerations we have reason to believe that an oxygen vacancy adjacent to a cobalt atom should compensate for only one electron charge at the cobalt site and leave an adjacent titanium atom with an "extra" electron. Otherwise, a titanium atom must give/share an electron to/with an oxygen atom that isn't a nearest neighbor, thereby likely inducing large lattice distortions, if even possible. Furthermore, a perfectly charge compensating vacancy as described above would not generate a polaron because there are no *extra* electrons loosely bound to a defect; all electrons are accounted for.

One can envision a situation where $Co_{Ti}^{2+}$ is uncompensated and thus leads to the formation of two holes (Figure 5.8b). Alternately, if isolated, cobalt atoms may adopt higher oxidation states (3+ or 4+). The 4+ oxidation state requires no compensation and generates no polaron (Figure 5.8f). The 3+ oxidation state may or may not be compensated. If not, we have $Co_{Ti}^{1+}$ (with one hole). If compensated by an oxygen vacancy, we then have $Co_{Ti}^{1+}$ and $V_O^{2-}$ which represents the combination of a substitutional cobalt, an oxygen vacancy, and an extra electron in a polaron state (Figure 5.8d). A cobalt ion in the 2+ oxidation state may be accompanied by two oxygen vacancies (Figure 5.8c). This is represented by $Co_{Ti}^{2+} + V_O^{2-} + V_O^{2-}$ and would result in two polarons. Finally, multiple $Co_{Ti}^{2+}$ defects may be interlinked by $V_O^{2-}$ defects (Figure 5.8e). This poses no geometrical quandaries, but may not lead to ferromagnetic ordering. The actual lattice response to a substitutional cobalt atom is expected to depend on the local concentration of cobalt atoms, oxygen vacancies, and other possible defects.

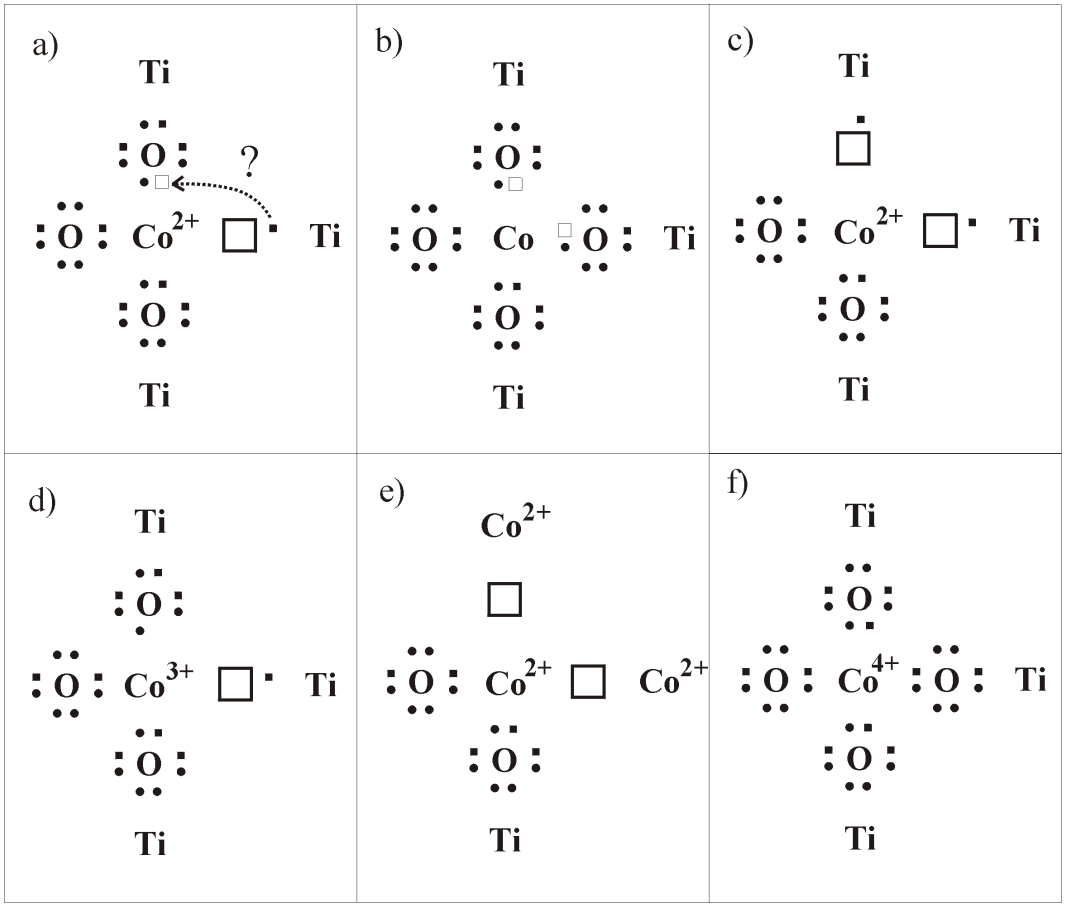


Figure 5.8. Possible crystal responses to substitutional cobalt atoms in the $TiO_2$ lattice. a) $Co^{2+}$ and associated oxygen vacancy; b) $Co^{2+}$ and two holes; c) $Co^{2+}$ and two O vacancies; d) $Co^{3+}$ and an O vacancy; e) chain of $Co^{2+}$ and oxygen vacancies; f) Co adopting the 4+ oxidation state.

One of the aforementioned situations could constitute the specific local environment that leads to the L* feature. In our opinion, a reasonable possibility is that the L* feature stems from a $Co_{Ti}^{1+}$ ($Co^{3+}$ substituting for a $Ti^{4+}$) and $V_O^{2-}$ combination in which the Co 3d states are hybridized with the s-like polaron orbital generated by the oxygen vacancy. This is, in fact, suggested as the ferromagnetic interaction magnetism by Coey[27] (once percolation is achieved at high enough concentrations). Cobalt 2p core electrons may then be excited to this hybridized orbital, or perhaps another hybridized orbital. The only way to validate such conjectures may be by theoretical calculations.

Vanishing of the L* Feature

The reasonable correspondence between the deduced defect size and the polaron radius, as well as the behavior of the L* feature intensity as a function of defect concentration makes a compelling argument that the feature is due to isolated cobalt atoms and associated polarons. Yet, one question remains regarding *why* only *isolated* defects lead to the feature. We see two possible explanations to this peculiarity and they may be related.

First, according to the polaron percolation model, at a certain polaron concentration threshold, the polarons percolate and lead to macroscopically observable ferromagnetism. There is a also critical donor concentration at which the impurity band states (polaron hydrogenic orbitals) become delocalized[70]. If the L* edge is indeed related to the localized polaron state, then upon delocalization, with polaron orbital energy levels spreading into bands, the sharp resonant transition leading to the L* edge may disappear. Note that in $TiO_2$, according to Coey *et al.*[27], delocalization occurs at a lower concentration than percolation. However, according to Kaminski *et al.*[31] delocalization is not necessary for ferromagnetism to emerge.

The second explanation, which does not exclude the first, is that the L* edge is an energy shifted L edge due to a different oxidation state and structural neighborhood of isolated cobalt atoms. As the concentrations of cobalt and/or oxygen vacancies increase, substitutional cobalt atoms can share oxygen vacancies, remain in the +2 oxidation state and yield the conventional XAS spectral shape characteristic of octahedrally coordinated $Co^{2+}$. The L* absorption then represents photon absorption by cobalt atoms in the unique configuration illustrated in Figure 5.8 d). A notable difference with the first explanation

is that without excluding delocalization, this second option does not require it. Only a small number of interconnected cobalt atoms and oxygen vacancies destroy the isolated quality of isolated atoms and lead to the disappearance of the L* feature. This interpretation corresponds more closely to the trend we observe in the L* feature. It is also very important to point out that the isolated nature of the cobalt atom is not the direct cause of the L* feature, because we have seen the feature in other systems, such as cobalt oxide nanoparticles (unpublished). However, the isolated nature of cobalt atoms in $TiO_2$ must facilitate the local chemical/structural environment that *is* responsible for the feature, whatever it may be.

## The L* Feature and the Magnetic Behavior

The final and perhaps most compelling evidence of the relationship between the L* feature and the polaron percolation theory comes when we perform a parallel study of the L* spectral component, the assumed isolated defect model, and the measured magnetic moment. As the cobalt concentration is increased, the L* spectral contribution follows a trend compatible with our model which attributes the L* component to isolated cobalt atoms and associated polarons. This agreement not only applies to the trend's functional form but also to the deduced defect size, which matches the polarons that are suggested to mediate the cobalt-cobalt interaction. Finally, as the fraction of isolated defects decreases, the number of percolating defect naturally increases. This is expected to result in an increase of the measured magnetic moment, as is verified by magnetic measurements by our collaborators. The results illustrating this point are presented in Figure 5.9. In this figure the L* spectral component is shown to follow the Monte Carlo

simulation carried out with 5.9 Å radius defects, as function of defect concentration. Concurrently, the magnetic moment per cobalt atom increases in an exponential fashion. Note that the L* component declines faster than the magnetic moment increases. This is in perfect accord with our expectations. At low concentrations, when defects begin to connect in small networks, they immediately lose their isolated quality, causing the decline of the L* spectral component. However, in order to generate macroscopically observable long-range magnetic order, the concentration must be high enough to generate a percolating phase within the sample.

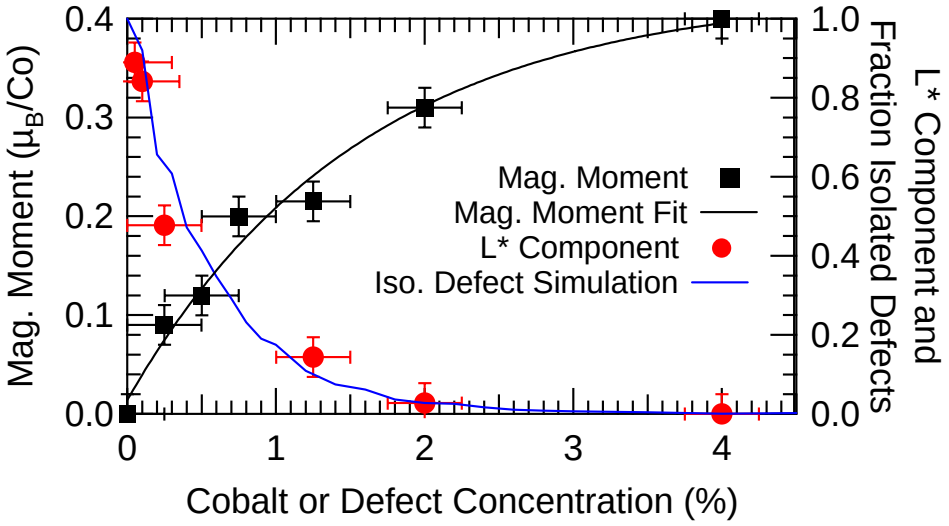


Figure 5.9. The magnetic moment per cobalt atoms, as measured by our collaborators, is plotted against the left axis. An exponential fit is included to demonstrate the trend. The L* spectral component and a Monte Carlo isolated defect simulation are plotted against the right axis. The Monte Carlo simulation was carried out with 5.9 Å radius defects.

# SUMMARY

## Conclusions

As room temperature ferromagnetic semiconductors, magnetically doped oxides are technologically valuable for applications in semiconductor spintronics. Our general goal was to understand how and why ferromagnetism occurs in these novel materials. For this endeavor, we concentrated on a material of considerable current interest, cobalt-doped titanium dioxide. To completely and unambiguously understand every aspect of this material would require several experimental techniques and supporting theoretical calculations. We did not, and could not, perform all this work. We concentrated on what we do well, which is the X-ray characterization of these materials. Our work, along with the knowledge gained from the work by others, allowed us to make significant contributions to the research community's understanding of this fascinating new material. By understanding, we mean becoming aware of the various forms in which this material may present itself, gaining an understanding of how preparation techniques and parameters affect the resultant material, understanding the effects of cobalt concentration on the resulting material, gaining insight in the magnetic behavior and the interaction mechanism responsible for the ferromagnetic behavior. Additionally, we aimed to understand the new and surprising observations that are particular to this material. These observations include the lack of XMCD in spite of the observed ferromagnetic behavior, and the presence of a new spectral feature in XAS. Understanding these unique properties, in turn, helps to address the previously mentioned issues.

Structural Characterization

Our XAS spectral characterization presented in chapter 2 shows how the various deposition parameters, specific to PLD samples affect the resultant film structure. The substrate-induced stabilization of the anatase phase is achieved if the substrate temperature is high enough to promote atomic mobility to conform to the substrate. Also, the substrate-induced anatase stabilization is effective for thin films (~ 2000 Å), but thicker films (~ 8000 Å) relax to the rutile structure as we move away from the substrate interface. The oxygen partial pressure must be high enough ($>1x10^{-5}$ Torr) to ensure successful growth. Post annealing in various gas environments has an important impact on the resultant film. Post annealing in vacuum causes expulsion of cobalt at the film's surface in clusters while it disperses the cobalt in the film's bulk. This is in agreement with the maximum solubility of about 2% claimed by our collaborators at the University of Maryland. Although the anatase phase has more wide-spread applications in electronics, and presumably in its future use in spintronics, the rutile phase is also a ferromagnetic semiconductor.

Magnetic Characterization

A few hysteresis loops measured by VSM show that the samples are indeed ferromagnetic with a coercive field of approximately 150 Oe. The same samples, however, have no XMCD signature. In light of the power of XMCD to probe magnetism with element specificity, the fact that no one has reported on XMCD measurements stands as a confirmation that this lack of XMCD is real and applicable to samples prepared by all techniques. Currently, we have no conclusive explanation for this surprising experimental observation.

L* Spectral Feature

We first observed the L* feature in our early efforts to characterize the Co-doped $TiO_2$ films. It quickly became apparent that this was a significant observation and that understanding the feature's origin could lead to a more complete understanding of the peculiar properties of DMSO. Our investigations on several samples to date have led us to the following conclusions. The feature is an absorption feature from cobalt atoms that are in a different structural and chemical state than those that give rise to the typical $Co^{2+}$ L edges. The isolation of those cobalt atoms in extremely dilute samples leads to the specific state responsible for the L* edge. This isolation is affected by the number of oxygen vacancies that allow dispersed cobalt atoms to effectively connect to one another. The effective radius with which they connect with one another is equal to the polaron radius that we expect in those materials. This helps confirm that the oxygen vacancies (which can constitute polarons), or other polaron inducing defects, are indeed what connects cobalt atoms to one another. Finally, the magnetic moment dependence on cobalt concentration is perfectly compatible with our description of the isolated-cobalt/oxygen-vacancy defects responsible for the L* feature. Hence, we have independently substantiated the polaron percolation mediated ferromagnetism theory in this material. This does not preclude the possibility of other interaction mechanisms operating simultaneously. The doped oxides have randomly distributed magnetic impurities in various concentrations, with various concentrations of oxygen vacancies and/or other defects, not to mention possible spatial variations in cobalt concentration. However, in the low dopant concentration regime our work demonstrates the clear role played by polarons in the magnetic interactions.

# Future Directions

## Polaron Radius Confirmation

It will be interesting to prepare samples of other cobalt-doped oxides to verify the polaron radius from the L* feature intensity. We have tabulated a list of possible oxide materials to dope with cobalt. These various oxides have various dielectric constants and various charge carrier effective masses giving them different polaron radii. By preparing samples of various cobalt doping concentrations of each of these oxides we can determine the effective defect radii and compare them to the calculated polaron radii tabulated below in below.

| Host Oxide | Dielectric Constant | Effective mass m*/m | Polaron Radius (Angst.) |
|---|---|---|---|
| $HfO_2$ | 25 | 0.1 | **132.5** |
| $ZrO_2$ | 20 | 0.3 | **35.3** |
| $In_2O_3$ | 9 | 0.3 | **15.9** |
| $SnO_2$ | 3.9 | 0.3 | **6.9** |
| $TiO_2$ | 9 | 1 | **4.8** |
| $SiO_2$ | 3 | 0.4 | **4.0** |
| ZnO | 2 | 0.3 | **3.5** |
| $BaTiO_3$ | 5 | 5 | **0.5** |
| $SrTiO_3$ | 5 | 5 | **0.5** |

Table 6.1. Table of various oxides, their dielectric constants, effective masses, and calculated polaron radius.

An easy and logical choice is to pursue the perovskite titanates (see Figure 6.1) because we've already observed the L* feature in Co-doped LSTO and also because the expected polaron radius is very small; therefore, we can expect to observe a large L* feature up to relatively large cobalt doping concentrations, making detection easy. Our preliminary results showing large L* features for 1.5% cobalt doping on LSTO provide

initial confirmation of our hypothesis. Additionally, this type of study is be interesting because it will help constrain our understanding of the origin of the L* feature. For example, if titanium is a necessary condition, because of hybridization with neighboring titanium atoms, perhaps through oxygen vacancies, the feature will not be observed in oxides that do not contain titanium. In light of our results, this does not appear to be the case but it would be useful to confirm it on a few systems.

The substitution of cobalt for a quadrivalent cation may be an essential condition for the appearance of the L* feature. For this reason, it will be interesting to experiment with co-doped ZnO, for which we would not expect to observe the L* feature. Another way to investigate valence effects that some groups have begun to explore is co-doping with higher valence cations such as chromium.

If the feature is observed in any of the systems listed in the table above, the next graph shows roughly the fractional L* intensity (equal to the fraction of isolated defects) as a function of defect concentration, that we should expect based on their polaron radii. One should keep in mind, when measuring samples, that the defect is somewhat loosely defined. As a first approximation, the defect concentration is equal to the cobalt concentration because we know these concentrations are correlated, based on local charge neutrality arguments. However, by independently varying the oxygen concentration or introducing other defects, the effective defect concentration can be increased, revealing itself as an apparent defect radius increase. This is immediately observable based on our oxygen partial pressure dependent study of Co-doped LSTO samples. Nonetheless, the table and figure should serve as a useful guideline. Recent work by several groups show

that defects play an important role in the observed ferromagnetism. We expect similarly important effects in the L* feature.

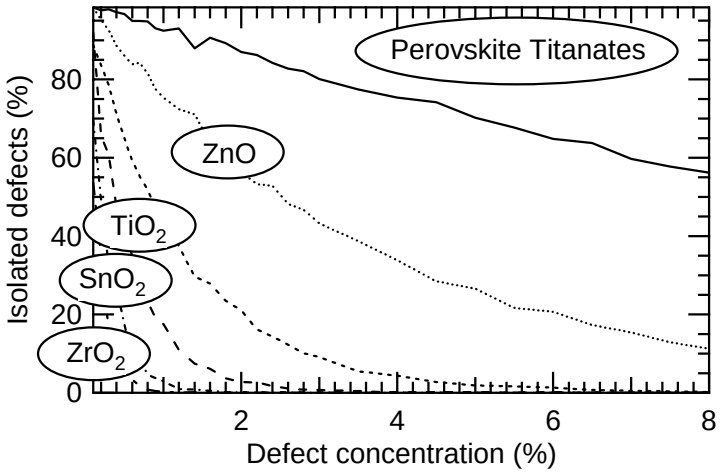


Figure 6.1. Expected L* feature fractional intensity trends expected for various co-doped oxides as a function of defect concentration, based on their calculated polaron radii.

XMCD (Lack of…)

The perplexing yet fascinating question of the absence of XMCD deserves additional attention. We have hinted to some possible explanations but many of them appear difficult to resolve. Namely, we suggest the magnetic moment could be carried by oxygen vacancy sites. If this is the case, an XMCD signal might be observable on the adjacent titanium atoms. However, the measurement does not distinguish between titanium atoms that are adjacent to vacancies and those that are not. The latter form an overwhelming majority and have a non-existent XMCD signature, making detection problematic. Perhaps very low noise and sensitive measurements could help make progress toward testing this hypothesis.

If the magnetic moment was carried by the cobalt atoms, based on the principles by which XMCD works, we should have detected it by now. Therefore, we must look for another carrier of the magnetic moments. The fact that several cobalt-doped oxides have proven to be ferromagnetic without showing an XMCD signature supports this idea.

## Closing Remark

Our current understanding of the mechanisms for ferromagnetism, the presence of the L* feature, and how they are related, converge into a consistent picture and make a compelling argument for the polaron percolation model. The several possible experiments outlined above will provide motivations for future students or other research groups to confirm our current understanding. The more precisely we understand these materials, the more effectively we can use them, and devise and tailor other materials into technologically useful spintronics devices.

REFERENCES CITED


[1] S. A. Wolf, Science **294**, 1488 (2001).

[2] S. Wolf, (2000), http://www.darpa.mil/DARPATech2000/Presentations/dso_pdf/3WolfSpinsB&W.pdf. Accessed Nov. 2005.

[3] J. A. C. Bland, Europhysics News **6**, 34 (2003).

[4] S. Datta and B. Das, Appl. Phys. Lett. **56** 665 (1990).

[5] F. G. Monzon, M. Johnson, and M. L. Roukes, Appl. Phys. Lett. **71**, 3087 (1997).

[6] G. A. Prinz, Physics Today **48** 58 (1995).

[7] H. Ohno, Appl. Phys. Lett. **69**, 363 (1996).

[8] H. Ohno, Science **281**, 951 (1998).

[9] P. LeClair, J. S. Moodera, and H. J. M. Swagten, in *Ultrathin Magnetic Structures*, edited by B. H. a. J. A. C. Bland.

[10] S. Johnson, Phys. Rev. B **58**, 9635 (1998).

[11] T. Dietl, Semicond. Sci. Technol. **17**, 377 (2002).

[12] Y. Matsumoto, M. Murakami, T. Shono, et al., Science **291**, 854 (2001).

[13] S. A. Chambers, S. Thevuthasan, R. F. C. Farrow, et al., Appl. Phys. Lett. **79**, 3467 (2001).

[14] J.-Y. Kim, J.-H. Park, B.-G. Park, et al., Phys. Rev. Lett. **90**, 017401 (2003).

[15] S. R. Shinde, S. B. Ogale, S. D. Sarma, et al., Phys. Rev. B **67**, 115211 (2003).

[16] S. A. Chambers, C. M. Wang, S. Thevuthasan, et al., Thin Solid Films **418**, 197 (2002).

[17] W. K. Park, R. J. Ortega-Hertogs, J. S. Moodera, et al., J. of Appl. Phys. **91**, 8093 (2002).

[18] S. B. Ogale, R. J. Choudhary, J. P. Buban, et al., Phys. Rev. Lett. **91**, 077205 (2003).

[19] Y. G. Zhao, S. R. Shinde, S. B. Ogale, et al., Appl. Phys. Lett. **83**, 2199 (2003).

[20] P. Sharma, A. Guptal, K. V. Rao, et al., Nature Materials **2**, 673 (2003).

[21] S. J. Pearton, C. R. Abernathy, M. E. Overberg, et al., J. of Appl. Phys. - Appl. Phys. Rev. **93**, 1 (2003).

[22] M. Venkatesan, C. B. Fitzgerald, and J. M. D. Coey, Nature (brief communications) **430** 630 (2004).

[23] D. C. Kundaliyai, S. B. Ogale, S. E. Lofland, et al., Nature Materials **3**, 709 (2004).

[24] R. I. Khaibullin, L. R. Tagirov, B. Z. Rameev, et al., J. Phys.: Condens. Matter **16**, L443 (2004).

[25] D. J. PriourJr., E. H. Hwang, and S. D. Sarma, Phys. Rev. Lett. **92**, 117201 (2004).

[26] F. Matsukura, H. Ohno, A. Shen, et al., PRB Rapid Communications **57**, R2037 (1998-II).

[27] J. M. D. Coey, M. Venkatesan, and C. B. Fitzgerald, Nature Materials **4**, 173 (2005).

[28] L. Bergqvist, O. Eriksson, J. Kudrnovsky, et al., Phys. Rev. Lett. **93**, 137202 (2004).

[29] M. A. Boselli, I. C. d. C. Lima, and A. Ghazali, Phys. Rev. B **68**, 85319 (2003).

[30] S. R. Shinde, S. B. Ogale, J. S. Higgins, et al., Phys. Rev. Lett. **92**, 166601 (2004).

[31] A. Kaminski and S. Das Sarma, Physical Review Letters **88**, 247202 (2002).

[32] T. Dietl, H. Ohno, F. Matsukura, et al., Science **287**, 1019 (2000).

[33] W. T. Geng and K. S. Kim, Solid State Communications **129**, 741 (2004).

[34] K. A. Griffin, A. B. Pakhomov, C. M. Wang, et al., Physical Review Letters **94**, 157204 (2005).

[35] T. Dietl, Europhysics News **34** (2003).

[36] P. Mahadevan, A. Zunger, and D. D. Sarma, Physical Review Letters **93**, 177201 (2004).

[37] S. A. Chambers, Materials Today, 34 (April 2002).

[38] A. Lussier, J. Dvorak, Y. U. Idzerda, et al., Physica Scripta **T115**, 623 (2005).

[39] A. Lussier, J. Dvorak, Y. U. Idzerda, et al., J. Appl. Phys. **95**, 7190 (2004).

[40] S. Hulbert, D. J. Holly, F. H. Middleton, et al., Nucl. Instrum. Method **A291**, 343 (1990).

[41] Y. U. Idzerda, V. Chakarian, and J. W. Freeland, Sync. Rad. News **10**, 6 (1997).

[42] V. Chakarian, Y. U. Idzerda, and C. T. Chen, Phys. Rev. B **57**, 5312 (1998).

[43] J. M. DeTeresa, A. Barthelemy, A. Fert, et al., Science **286**, 507 (1999).

[44] S. Stadler, Y. U. Idzerda, Z. Chen, et al., Appl. Phys. Lett. **75**, 3384 (1999).

[45] I.-B. Shim, S.-Y. An, C. S. Kim, et al., J. of Appl. Phys. **91**, 7914 (2002).

[46] Amethyst Galleries Inc., http://mineral.galleries.com/minerals/oxides/anatase/anatase.htm. Accessed Sept. 2005.

[47] H. Tang, Solid State Commun. **92**, 267 (1994).

[48] A. Kay and M. Gratzel, Sol. Energy Mater. Sol. Cells **44**, 99 (1996).

[49] Y. Matsumoto, M. Murakami, T. Hasegawa, et al., Appl. Surf. Sci. **189**, 344 (2002).

[50] M. Murakami, Y. Matsumoto, K. Nakajima, et al., Appl. Phys. Lett. **78**, 2664 (2001).

[51] J. Smyth, http://ruby.colorado.edu/~smyth/min/tio2.html, Accessed Sept. 2005.

[52] F. M. F. deGroot, M. Abbate, J. vanElp, et al., J. Phys.: Condens. Matter **5**, 2277 (1993).

[53] F. M. F. deGroot, J. C. Fuggle, B. T. Thole, et al., Phys. Rev. B **42**, 5459 (1990).

[54] R. Russ, A. Kikas, A. Saar, et al., Solid State Communications **104**, 199 (1997).

[55] L. Soriano, P. P. Ahonen, E. Kauppinen, et al., Monatshefte für Chemie **133**, 849 (2002).

[56] D. H. Kim, J. S. Yang, K. W. Lee, et al., in *Cond-mat*, 2002), Vol. 2005.

[57] J. R. Simpson, H. D. Drew, S. R. Shinde, et al., Physical Review B **69**, 193205 (2004).

[58] Ç. Kiliç and A. Zunger, Phys. Rev. Lett. **88**, 095501

[59] B. G. Lewis and D. C. Paine, MRS Bulletin **25**, 22 (2000).

[60] H. L. Hartnagel, A. L. Jain, and C. Jagadish, *Semiconducting Transparent Thin Films* (IOP Publising, Bristol, 1995).

[61] M. Berciu and R. N. Bhatt, Phys. Rev. Lett. **87**, 107203 (2001).

[62] J. König, H. Lin, and A. H. MacDonald, Phys. Rev. Lett. **84**, 5628 (2000).

[63] S. Krishnamurthy, C. McGuiness, L. S. Dorneles, et al., To be published in JAP (2005).

[64] F. M. F. de Groot, J. Faber, J. J. M. Michiels, et al., Phys. Rev. B **48**, 2074 (1993-II).

[65] S. A. Chambers, S. M. Heald, and T. Droubay, Phys. Rev. B **67**, 100401(R) (2003).

[66] A. Kaminski, V. M. Galitski, and S. D. Sarma, Physical Review B **70**, 115216 (2004).

[67] J. M. D. Coey, A. P. Douvalis, C. B. Fitzgerald, et al., Applied Physics Letters **84**, 1332 (2004).

[68] J. M. D. Coey, in *Magnetism and Magnetic Materials Conference*, 2004), p. Oral communication.

[69] N. F. Mott, *Metal-Insulator Transitions* (Barnes & Nobles Books, New York, 1974).

[70] N. F. Mott, *Conduction in Non-Crystalline Materials* (Oxford University Press, New York, 1987).

[71] G. Cangiani, (École Polytechnique Fédérale de Lausanne, Lausanne, 2003), Vol. Doctoral Dissertation, p. 97.

[72] R. Zallen, *The Physics of Amorphous Solids* (John Wiley & Sons, New York, 1983).

[73] J. Okamoto, H. Miyauchi, T. Sekine, et al., Phys. Rev. B **62**, 4455 (2000-I).